# Politecnico di Torino

Master's Degree in Mechanical Engineering


Master's Degree Thesis

# Development and integration of actuating and sensing subsystems of scaled wind turbines for wind tunnel testing

Supervisors

Prof. Giovanni BRACCO

Ph.D. Filippo CAMPAGNOLO

Candidate

Matteo PROTASE

October 2024

# Acknowledgements

Vorrei innanzitutto ringraziare il Professor Giovanni Bracco e la Professoressa Maria Pia Cavatorta per il supporto e la guida preziosa durante questi ultimi mesi, così come Filippo Campagnolo e tutto l'LWE della TUM di Monaco di Baviera per avermi dato la possibilità di scrivere questa tesi nel loro dipartimento e di aver potuto lavorare ad un progetto tanto formativo quanto stimolante che mi ha fatto scoprire ed entrare nel mondo dell'energia eolica.

Il ringraziamento più grande va ovviamente a mamma e papà, i quali mi hanno spronato e sostenuto da sempre e non smetteranno mai di farlo.

Vorrei esprimere poi il mio più grande affetto e riconoscenza a tutti gli amici e le persone che mi hanno accompagnato in questo percorso universitario, partendo da quelli di vecchia data con cui sono cresciuto e che sono rimasti sempre al mio fianco, passando a quelli che ho incontrato durante questi 5 anni e con cui ho condiviso tutte le gioie e i sacrifici di questo viaggio, per finire poi col meraviglioso gruppo trovato a Monaco e col quale ho vissuto un'esperienza straordinaria che porterò per sempre nel cuore. Un ringraziamento speciale va ovviamente a Daniele, col quale in questi ultimi 6 mesi ho condiviso praticamente tutto, consapevole del legame fraterno creatosi e che ci legherà per sempre.

I miei ringrariamenti vanno inoltre a tutta la mia famiglia e ai parenti che mi sono stati vicini e mi hanno supportato più di quanto non mi sarei mai potuto aspettare dandomi tutto il loro affetto e i loro consigli.

Matteo

# Abstract

INSTITUTE FOR WIND ENERGY

The following thesis presents the work carried out by myself during the last 6 months in the Chair of Wind Energy (LWE) at TUM University. This project gave me the opportunity to step into the world of scaled wind turbines and their potential and applications in wind tunnel test scenarios, with a specific focus on the mechatronic features, subsystems and components. The work campaign consisted of three main related topics. A first results validation has been performed regarding a new multi-hole pressure probe through post-processing of experimental data previously acquired with the aspiration of implementing such a new sensor on each model in the Chair. Then, two different wind turbine models, the G1 and the G06, were investigated with a complete discussion of their characteristics, followed by a walkthrough of their assembly processes from scratch, their calibrations and the validation of the new technical improvements recently implemented. The culmination of this work consisted of the two wind tunnel test campaigns conducted in May and July. During the first one, new dynamic control strategy variants for wind farms optimization have been investigated to contribute to the growth of the state of the art of the Helix theory through DIPC control technique and evaluate new possible frontiers. The second campaign instead, had the purpose of accessing the performance and control strategy curves of the improved models to confirm and validate their reliability, functioning and characteristics.

# Table of Contents

# List of Figures

# Acronyms

**FA** Fore-Aft moment

**SS** Side-Side moment

**AoI** Angle of incidence of airfoils and blades

**AoA** Angle of attack of airfoils and blades

$\boldsymbol{\beta}$ Pitch angle

$\boldsymbol{\gamma}$ Yaw angle

**DIPC** Dynamic Individual Pitch Control

**Ti** Turbulence intensity

**St** Strouhal number

**TSR** Tip Speed Ratio

**CFD** Computational Fluid Dynamics

**FEM** Finite Elements Method

**a** Induction factor

$\mathbf{C}_P$ Power coefficient

$\mathbf{C}_T$ Thrust coefficient

# Chapter 1

# INTRODUCTION

## 1.1 Motivations

The global energy production landscape has undergone a radical revolution over the past few decades, driven by the urgent need for sustainable and clean energy sources due to the global warming crisis. The indisputable effects of climate change have forced worldwide governments and political organizations to integrate climate mitigation objectives into their policies, in particular regarding the rise of global temperatures. According to the United Nations, a 7.6% annual reduction in greenhouse gas emissions is required between 2020 and 2030 to limit global warming to 1.5°C. [1] This has therefore intensified the focus on renewable energy sources, intending to limit the use of fossil fuels as far as possible toward more sustainable alternatives, such as solar photovoltaic, wind offshore and onshore turbines and nuclear power plants. For what concerns the European Union, building on the 20% target for 2020, the recast Renewable Energy Directive 2018/2001/EU established a new binding renewable energy target for the EU for 2030 of at least 32%. The revised Renewable Energy Directive EU/2023/2413, after the launch of the REPowerEU Plan, raised later the EU binding renewable target for 2030 to 45%, aiming to reduce European CO2 emissions by up to 60%. [2] [3] This project, as ambitious as it is necessary, aims therefore to almost double the existing share of renewable energy production in the EU. Figure 1.1 and 1.2 illustrate the public electricity generation sources in the European Union for 2023.

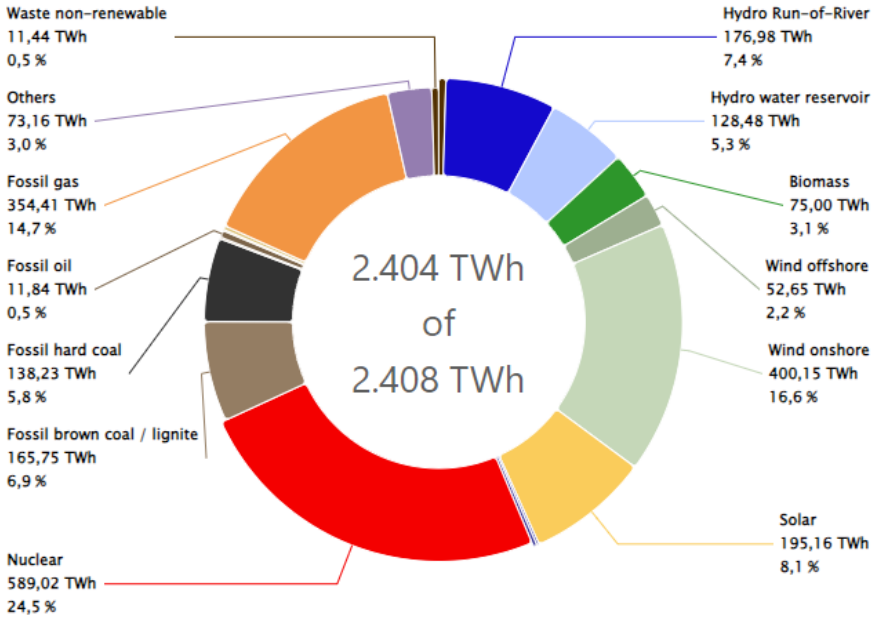


**Figure 1.1:** Public net electricity generation in the European Union in 2023 [4]

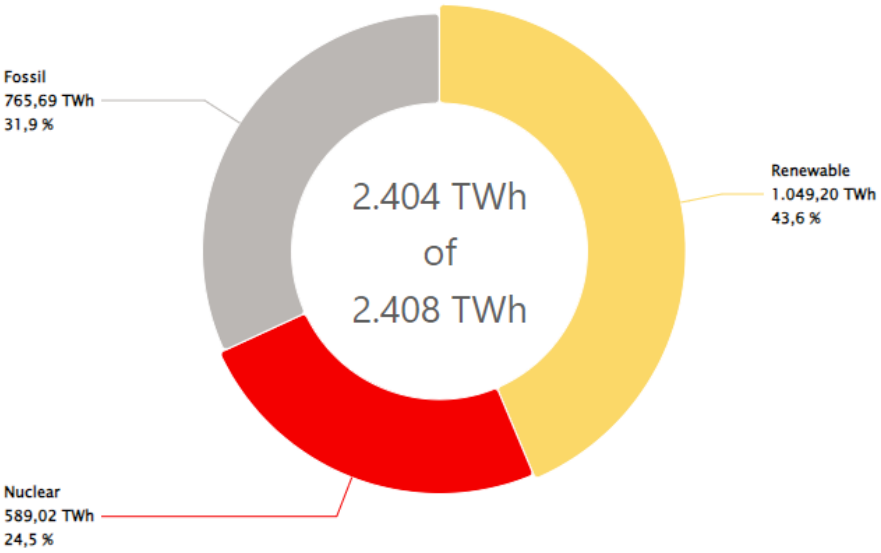


**Figure 1.2:** Net electricity generation share in the European Union in 2023 [4]

The wind energy sector is one of the most relevant renewable energy sources due to its availability and achievability of extraction and as a result, it has become a major player in the global energy sector in the last decades. Figure 1.3 displays his

incredible development through the cumulative global installations for onshore and offshore wind turbines in Gigawatts [GW]. The amount of installed capacity has grown by 3000 % since 2001, especially thanks to new technology achieved in this sector by government subsidies and boosted investments. [5]

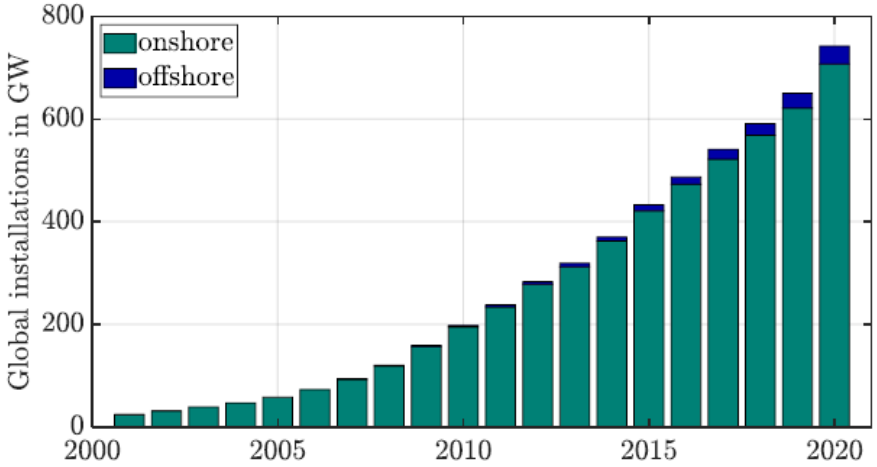


**Figure 1.3:** Wind energy installations in [GW] [5]

Wind turbines are typically arranged in wind farms due to the numerous advantages that this configuration offers, such as reduced maintenance costs, easier grid connectivity and decreased land use, which usually represents the bigger issue in terms of installation costs and licenses. To maximize the efficiency of these sites, the optimal adopted distance between turbines in a wind farm is generally around 15 times the rotor diameter (15 D). However, in dealing with modern wind turbines that exhibit rotor diameters of up to 200 meters, especially in offshore models, this ideal spacing turns out to be often impractical due to the extensive land requirements. Consequently, wind farms typically implement a spacing of around 6-10D among turbines to minimize costs and land use. However, this closer spacing introduces challenges and drawbacks, particularly regarding the wake interactions. The wake is defined as the area behind a wind turbine characterized by reduced wind velocity and increased turbulence, which significantly impacts downstream models. In the worst-case scenario, turbines positioned directly behind others with respect to the main flow direction can experience up to a 40% loss in energy extraction and increased fatigue loads due to insufficient wake recovery.[6][7]

To tackle these challenges, researchers are focusing on developing and optimizing new wake control techniques for wind farms, such as dynamic yaw or DIPC, through computer simulations (CFD and FEM usually), wind tunnel tests with scaled turbine models and, when achievable, full-scaled evaluations.

## 1.2 Scaled wind turbine models and wind tunnel tests

The development of scaled wind turbine models represents the conjunction ring in the wind energy research field between computer simulations, such as Large Eddy Simulations (better known as LES), and field testing with real-scale turbines. The research community has developed a huge interest in small-sized models in the last decades because of their capability to recreate full-size characteristics and behaviour in wind tunnels where many tests can be performed. Indeed multiple test conditions can be implemented to suit perfectly the desired experimental goals with a lower amount of expenses, time and effort compared with real-world scenarios. Despite the capability to recreate tailored circumstances, the non-dimensional parameters of scaled models often differ from the full-sized ones and not all the real scenarios and phenomena, especially ones regarding complex wake developments or turbulent flux mixing, typical of the atmosphere, induced by the morphology or unpredictable meteorological events. More specifically, scaled wind turbines are capable of reproducing the aerodynamics accurately, or how the air fluxes behave around the turbine, and the aeroelasticity, or how turbine structures react to aerodynamic forces, even if it results however way more complex to be simulated and reproduced. [8]

The different models designed and assembled in Chair suit perfectly therefore the aim of investigating the formation and development of complex wakes and the implementation and test of multiple control techniques for wind farm scenarios. Moreover, they allow us to observe how machines behave in particular operating conditions, such as extreme yaw or pitch angles that could be needed during emergencies, or to evaluate the different loads that affect structures during complex control techniques. [8] The combination of aeroelasticity models and wind tunnel testing allows more than immediate benefits, driving innovation and advancing research in wind energy technology. As wind turbines progress in complexity and full-scale reproduction capacity, these methods allow for the enhancement of design strategies, validation of performance forecasts, and the optimization of new control systems, consequently supporting the ongoing growth and development of the wind energy sector.

To summarize, scaled models offer the best cost-effective approach to replicating real-world conditions, allowing developers, researchers and engineers to evaluate pioneering design configurations, assess performances and tackle control challenges avoiding the financial and operational risks of full-scale deployments.

## 1.3 Scaled design criteria

The two models employed in this thesis, the G06 and G1, are both derived from the same full-scale model, the DTU 10 MW. It is an onshore model, achieving a rated power of 10 MW, featuring a rotor diameter of 178.3 m, an optimum TSR $\lambda_{\text{opt}} = 8$, and a rated wind speed of 11.4 $\frac{\text{m}}{\text{s}}$. [9] To guarantee a perfect kinematic flow similarity, or geometrically similar flow streamlines, the TSR of the two turbines must match. The Tip Speed Ratio (TSR or $\lambda$) for wind turbines is defined as:

$$\text{TSR} = \frac{V_{\text{tip}}}{U} \tag{1.1}$$

where:

- $V_{\text{tip}}$ is the linear speed of the turbine blade tip.
- $U$ is the wind speed.

In terms of the rotational speed $\Omega$ [$\frac{\text{rad}}{\text{s}}$] and the rotor radius $R$ [m], the tip speed $V_{\text{tip}}$ can be expressed as:

$$V_{\text{tip}} = \Omega R \tag{1.2}$$

Thus, the TSR is usually written as:

$$\text{TSR} = \frac{\Omega R}{U} \tag{1.3}$$

This is a critical parameter in the design and performance of wind turbines since each device operates optimally in a certain range of TRSs to guarantee maximum efficiency enhancing the energy extracted from the wind and minimizing mechanical stresses and noise. Usually, according to the mean wind intensity that the turbine will experience in normal operating conditions, or design conditions, a proper rotor dimension and speed are selected to guarantee the maximum efficiency. [10]
Concerning instead the dynamic flow similarity, it would entail a match between the ratio of the forces acting on the model and on full-scale devices. This condition is more difficult to achieve, as it would require matching the chord-based Mach and Reynolds numbers. However, reaching higher wind speeds in the confined environment of a wind tunnel turns out to be challenging since constraints arise from spatial limitations. Consequently, while for the Mach number, it is sufficient to guarantee that an upper bound is not exceeded to avoid compressibility effects [11], for what concerns Reynolds number the situation reveals trickier and therefore a degree of mismatch must be accepted. Specifically, the achieved Reynolds number in the wind tunnel is notably lower than the actual one in practical scenarios. In order to mitigate this discrepancy, it has been decided to adopt specialized

low-Reynolds airfoil profiles to compensate for the impact of this effect. Moreover, in terms of loads and structural excitations, two further conditions have been imposed during design for a perfect scaled-down. Firstly, consistency in the Lock number, an adimensional key factor that ensures an equivalent ratio of aerodynamic and inertial forces, and lastly also the non-dimensional natural frequencies of the structures must match to guarantee similar dynamic behaviours and associated harmonic excitations and resonances. [8]

## 1.4 Objectives

As introduced previously in the Abstract, this project aims to give an insight into the scaled wind turbines world and their potential in wind tunnel test scenarios. Two different models have been used, with a complete discussion of their characteristics, followed by a walkthrough of their assembly processes from scratch, their calibration and validation of the new technical improvements recently implemented. The culmination of this work consists of the two wind tunnel test campaigns conducted in May and July. The first one aimed to explore new variants of the Helix theory through DIPC in a partially-bladed version and combined with derating, basically one of the new frontiers of wind farm dynamic controls. The second had the purpose instead of accessing the performance and control strategy curves of the improved models to confirm and validate their reliability, their functioning and all the work made on them in the previous months. Lastly, the characteristics of a new multi-hole probe for wind speed and direction detection have been explored through the post-processing of experimental data previously acquired with the aspiration of implementing such a new sensor on each model in the Chair.

# Chapter 2

# FUNDAMENTALS

The following chapter aims to provide the necessary theoretical background to allow the best understanding of all the topics discussed after and the tests campaigns performed, with a focus on the characteristics that define turbine performances and on the modern control techniques for wind farms.

## 2.1 Performance evaluations

The flow around a wind turbine presents a huge complexity, exhibiting three-dimensional, time-dependent and turbulent behaviour, with vortice generation in the wake. To deal with such a topic, simplifications and approximations must be often applied in flow analysis, depending on the specific focus and depth of the study. The energy extraction mechanism from the wind by the turbine is typically described using basic stream-tube analysis, which considers the flow as one-dimensional, in steady state, inviscid, and irrotational. Furthermore, the wind turbine has been modelled as a permeable thin disk with the same diameter as the rotor to facilitate the analysis. Based on what was just discussed, the one-dimensional stream tube theory is based on the conservation of mass, momentum, and energy and it is illustrated in Figure 2.1, where $U_0$ and $p_0$ represent the flow velocity and pressure at the beginning of the stream tube, $U_{disc}$ the flow velocity at the rotor disc, $U_{inf}$ is the wind speed of the free stream and $U_1$ and $p_1$ the velocity and pressure after the rotor disc. The upstream zone is denoted as the induction zone while the downstream one is identified by the wake. [12] [10]

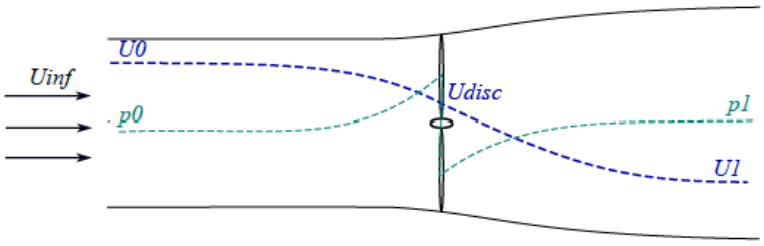


**Figure 2.1:** 1-D stream tube theory [12]

The blue dashed line, representing wind speed, decreases as the turbine extracts kinetic energy from the wind. Due to the conservation of mass in the stream tube, the velocity difference leads the streamlines to diverge, leading to an expansion of the wake and a rise in the air pressure (green dashed line) just before passing the rotor and dropping abruptly when the flow reaches it. The upstream aerodynamic effect due to the turbine's presence is called the blockage effect and it is responsible for losses in power extraction. Applying the energy conservation principle to the control volume, it is possible to evaluate the amount of power [W] that the turbine is able to extract and represented by the following equation: [10]

$$P = \frac{1}{2}\rho U_{disc} A \left(U_{inf}^2 - U_1^2\right) = \Omega Q \tag{2.1}$$

with $\rho$ $[\frac{\text{kg}}{\text{m}^3}]$ as the air density, $A$ $[\text{m}^2]$ as the rotor area and $\Omega$ $[\frac{\text{rad}}{\text{s}}]$ and Q [Nm] as the rotor speed and torque. The wind speed at the rotor disc $U_{disc}$, is defined as follows:

$$U_{disc} = \frac{1}{2}\left(U_0 + U_1\right) \tag{2.2}$$

$U_{disc}$ is naturally lower than $U_{inf}$, due to the expansion previously explained and their gap is described by the induction factor a:

$$a = \frac{U_{inf} - U_{disc}}{U_{inf}} \tag{2.3}$$

Moreover, another relevant quantity is represented by the thrust force $T$ [N] that the rotor exerts on the wind and is described as:

$$T = 2\rho A U_{inf}^2 a\left(1 - a\right) \tag{2.4}$$

Some adimensional parameters have been introduced to evaluate the efficiency of wind turbines. The principals are represented by the Tip-Speed Ratio (previously presented) and by the power $C_P$ and thrust $C_T$ coefficients. [10]

$$\mathrm{TSR} = \frac{\Omega R}{U} \tag{2.5}$$

$$C_P = \frac{P}{\frac{1}{2}\rho U_{inf}^3 A} = 4a\,(1-a)^2 \tag{2.6}$$

$$C_T = \frac{T}{\frac{1}{2}\rho U_{inf}^2 A} = 4a\,(1-a) \tag{2.7}$$

The TSR is a critical parameter that correlates the rotational speed of a wind turbine's blades with the approaching wind speed and it is usually adopted as a fundamental design factor, considering that it impacts the turbine aerodynamic and geometrical efficiency. The two coefficients instead, respectively quantify the fraction of the wind's kinetic energy that can be captured and converted into electrical power ($C_P$) and the fraction of the wind's momentum that is intercepted and converted into thrust by the wind turbine ($C_T$ ).
It must also be specified that the maximum power extractable by a turbine from the wind energy density that passes the stream tube exhibits a maximum. This represents a limit, that in terms of power coefficient is $C_P = 16/27 \simeq 0.593$ for an induction factor of a $= \frac{1}{3}$ and is known as the "Betz Limit". [10] [13]

### 2.1.1 Performance curves

During a turbine design, it is evident that the aim is to maximise as possible the power extracted by it, meaning to operate in the most performance conditions that depend on the design parameter adopted. ($C_P$ ) and ($C_T$ ) are so deeply investigated to achieve the right balance between capturing as much wind energy as possible while guaranteeing that the turbine operates safely and efficiently. A graphical representation of this is usually provided by two extremely relevant curves identified as performance curves: $C_P$ vs TSR and $C_T$ vs TSR. These curves illustrate how efficiently a wind turbine operates and the points where energy extracted is maximized. These coefficients strongly depend also on another important parameter, the pitch angle $\beta$. It is defined as the angle between the airfoil's chord line and the rotor disc's plane and impacts the power extraction and the thrust intercepted since it modifies the lift generated by the blades as airfoils. [10]

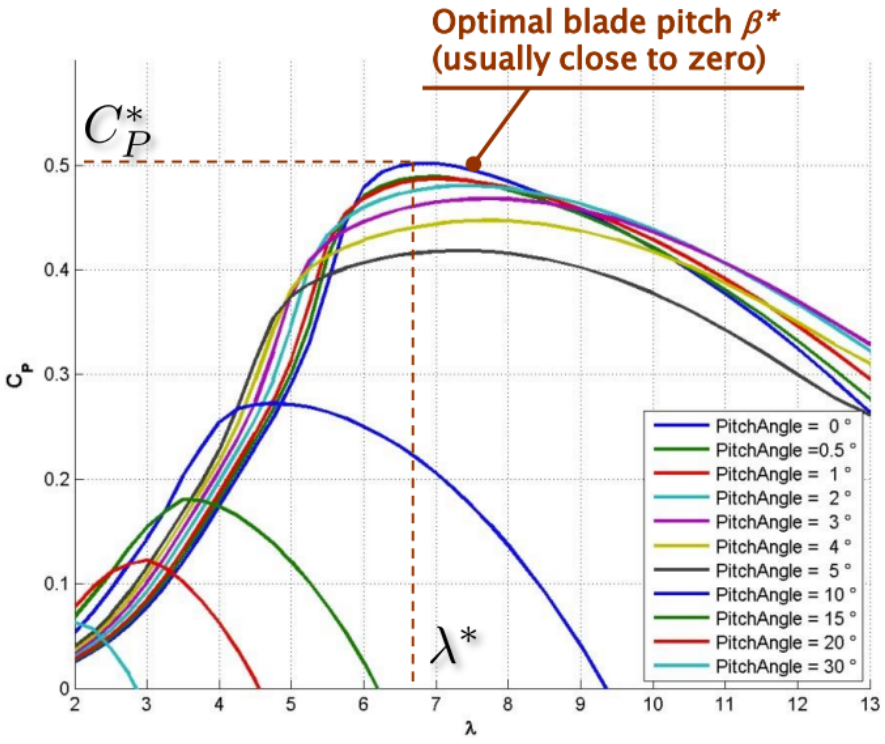


**Figure 2.2:** $C_P$ vs TSR [14]

While the TSR is normally modified by the surrounding conditions, such as wind speed variations, the pitch angle represents one of the most important controls available in wind turbines, since it allows to work with the best $C_P$ in different TSR conditions or intentionally reduce the power extraction working in non-optimal conditions. Basically, the lift produced by the rotor blades results lower when operating at not-optimal pitch angles, consequently, the generated torque and the power that can be extracted diminish: the machine undergoes a partial force unload. This strategy takes the name of "derating" and, as it will be explained in the following sections, plays a fundamental role in wind farm control where the interactions among turbines become crucial. [14]

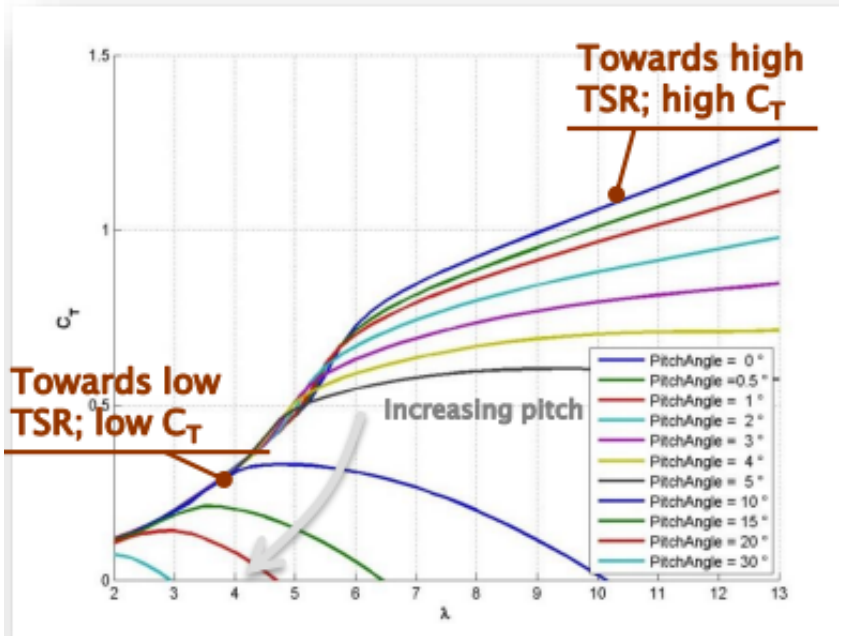


**Figure 2.3:** $C_T$ vs TSR [14]

### 2.1.2 Control strategy curves

To access the optimal turbine's control strategies, a batch of other four key curves is normally analysed. These curves depict power, torque, pitch, and rotor speed (or often $\lambda$) behaviours against the wind speed.

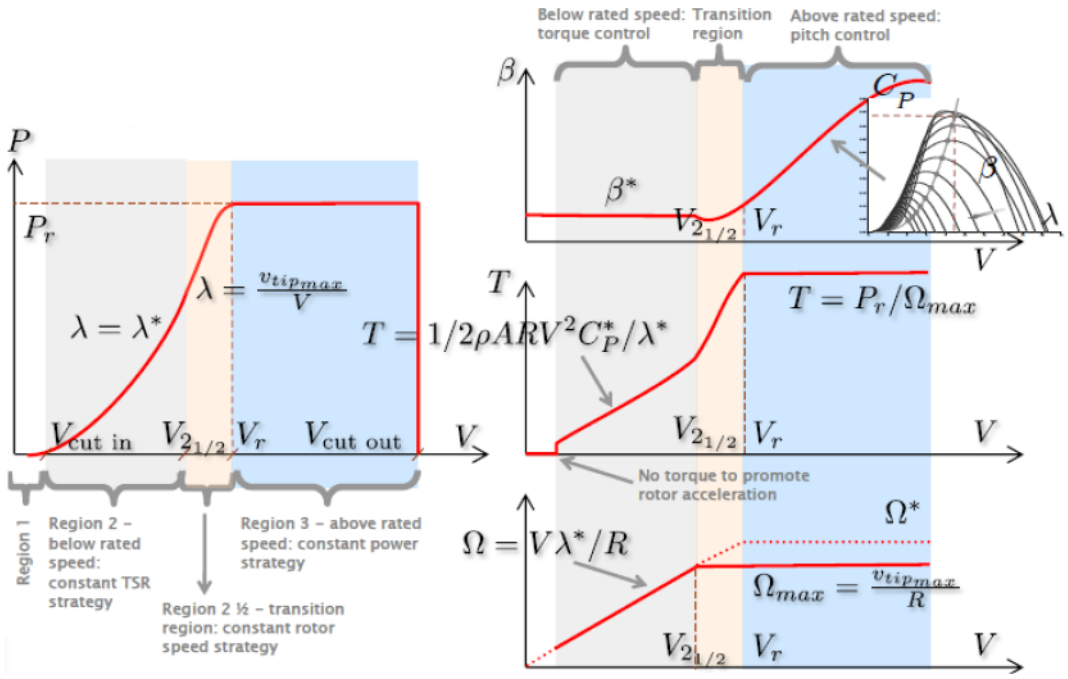


**Figure 2.4:** Control strategy curves [14]

Figure 2.4 depicts the three distinct regions present, each of them characterized by a different operational phase and control strategy.

- **Region 1**: The wind speed is lower than the cut-in speed $V_{cut-in}$ (the minimum speed that causes the rotor to spin) and the turbine is still and $\Omega$ and power extracted are zero.
- **Region 2**: The wind speed overcome the $V_{cut-in}$ and the torque results enough to propel rotor acceleration. The wind turbine operates at constant design $\lambda^*$ to guarantee the design maximum power coefficient $C_p^*$. Therefore, the rotor speed is modified according to wind speed.

$$\Omega = \lambda^* \frac{R}{V} \tag{2.8}$$

The torque $Q$ increases with wind speed according to Equation 2.9.

$$Q = \frac{1}{2}\rho A R V^2 C_p^* \lambda^* \tag{2.9}$$

The pitch angle remains unchanged at optimal value $\beta^*$ to maximize $C_p^*$.

- **Region 2($\frac{1}{2}$)**: The rotor speed reaches its maximum rated value $\Omega_{\max}$, which is constrained by the maximum tip speed $v_{\text{tip,max}}$. If the wind speed rises, $\lambda$ changes according to Equation 2.10.

$$\lambda(V) = \frac{\Omega_{\max} R}{V} \tag{2.10}$$

- **Region 3**: When the wind turbine reaches its rated output power $P_{\text{rated}}$, the pitch actuator turns on and increases the blade pitch angle $\boldsymbol{\beta}$, reducing the power extracted by the turbine and consequently the coefficient $C_p$ to keep constant the power output. This operation aims to avoid exceeding the rated maximum power of the device, which could induce overloads capable of damaging the turbine's components.

To summarize, a different control strategy results mainly suitable for each region, starting with the constant TSR*, proceeding with constant $\Omega_{\max}$ and concluding with constant power $P_{\text{rated}}$. [14]

## 2.2 Modern control techniques in wind farms

As previously introduced, dealing with wind farms represents the ultimate challenge and frontier in the wind energy field since multiple factors and phenomena must be taken into account with respect to the control of single turbines. Firstly it must be understood that concerning multiple turbines with closer spacing, the main focus is no more represented by the singular performances but on how the full site behaves and how the machines interact and create disturbances among them. Therefore, modern research considers the following as main goals:

- Increase the power extraction
- Reduce the structural loads on the turbines
- Support the grid stability and the auxiliary services
- Optimize operation and maintenance of wind turbines
- Mitigate as possible the environmental and social impacts

The most problematic issue is represented by the wake effect, or how multiple turbines behave and are affected by the wakes of turbines located upstream. This complex flow region is derived from the energy extracted by a rotor and has a strong impact on performances and load management for downstream turbines. The next sections will briefly introduce this complex and challenging phenomenon and an overview of the main control strategies actually adopted and under research will be presented. [15]

### 2.2.1 Wake characteristics and recovery

When kinetic energy is extracted by a turbine from a free airflow, this interaction causes a drop in pressure immediately after the rotor section that leads to the generation of a region of lower flow speed and higher turbulence, commonly named wind turbine wake. As it flows downstream, it interacts with the surrounding free stream and gradually reduces the velocity and pressure deficits and the turbulence difference thanks to the vortex dissipation. This phenomenon is clearly presented in Figure 2.5, showing the so-called wake expansion as it moves away from the turbine. [16]

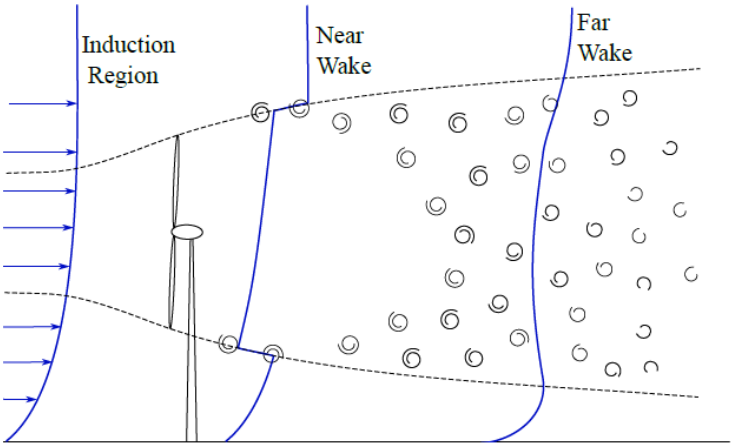


**Figure 2.5:** Turbine wake expansion [16]

The wake can be divided into two distinct regions: the near wake and the far wake. The first one, which extends approximately 2-4D downstream, is directly influenced by the rotor's shape and the blades' aerodynamics. It is characterized by high turbulence and the formation of vortices due to power extraction. These latter inhibit turbulent mixing and retard wake expansion. The far wake instead is where the mixing with the free stream begins and it develops after at least 4D. In this region, vortices start to break down, the velocity and pressure deficit decrease and the wake begins to recover. [16]
Recent researches indicate that the recovery characteristics of a wake depend on multiple factors, such as surrounding wind speed, turbulence levels, additional turbulence generated within the wake, geometry and design of the turbine, the adjacent orography and the structure of the atmospheric boundary layer.
Basically, the aim is to enhance the mixing of the wake region with the surrounding free flow to achieve the re-energization of the wake, promoting an earlier breakdown of vortices and thus accelerating its recovery. The stability and behaviour of these vortices have been the subject of detailed studies in the last years thanks to advanced CFD simulation as LES. Vortex instability indeed, arises from small perturbations that disrupt the symmetry of the vortices, leading to their eventual breakdown. [17]

### 2.2.2 Wind farm control strategies

In wind farms, this crucially impacts the performance and longevity of downstream turbines since those located within the wake of upstream machines experience reduced wind energy and increased turbulence, resulting in lower power output and higher loads. Fortunately, acting on the principal control regulation of a turbine has an impact on the wake behaviour and dynamics and particular strategies can be adopted to promote a faster wake recovery. [15]
The main regulations in a wind turbine are:

- **Yaw control $\gamma$:** The turbine rotor can be oriented horizontally to modify its alignment with the main wind direction. As expected, the higher the misalignment, the lower the power extracted due to worse lift generation conditions
- **Pitch control $\beta$:** Blade pitch angle can be modified both individually or collectively to modify their AoA and therefore the lift and torque generated by the rotor

Considering the worst-case scenario in which two turbines are almost perfectly aligned to the main wind direction, so basically with the upwind turbine covering the downwind one, the main concept behind these control strategies is the following. If no control is adopted, the front one will work practically undisturbed while the back one will experience all the wake and turbulences generated by the first one with a huge performance drop and load increment. Instead, the adoption of control strategies acting on the turbine's main regulations allows to achieve a complex power extraction value that is higher with respect to the case in which no regulations are implemented. This consists of a partial de-powering, or derating, of the upstream turbine that leads to an alteration of the wake behaviour behind it for the benefit of the downstream turbine, since it results able to produce more power with respect to experiencing the unmodified wake. Therefore, the aim is that globally the power extracted by the two turbines combined results higher with respect to the un-controlled scenarios. Despite the power loss by the upwind turbine, the gain that the downwind one obtains is way higher, leading to a higher global power extraction. It must be specified that implementing advanced control techniques means dealing with more complex systems and architectures that must be integrated, as well as higher component stress and wear that consequently lead to higher maintenance and control expenses, especially for dynamics techniques. Therefore, accurate technical and economic valuations must be conducted case-by-case. The next sections will briefly describe the most relevant control techniques in modern wind turbines, starting with the static approaches and then illustrating the more complex dynamic ones. In static control, the turbine parameters are modified according to the environmental conditions and the goals and maintained constant. On the other hand, dynamic control involves the constant adjustment of wind turbine parameters based on wake mixing and manipulation techniques. [15]

<table>
<tr><th></th><th>Static</th><th>Dynamic</th></tr>
<tr><td rowspan="2">Pitch</td><td rowspan="2">Static Induction Control (SIC)</td><td>Dynamic Induction Control (DIC)</td></tr>
<tr><td>Dynamic Individual Pitch Control (DIPC or Helix)</td></tr>
<tr><td rowspan="2">Yaw / Platform</td><td>Horizontal Steering</td><td rowspan="2">Dynamic Yaw Control</td></tr>
<tr><td>Vertical Steering</td></tr>
</table>

**Figure 2.6:** Control techniques outline

### 2.2.3 Static Induction Control

The Static Induction Control (SIC) strategy, also known as axial-induction control, is one of the earliest and basic techniques explored to improve the efficiency of wind farms. This strategy consists of altering the induction factor a, which correlates the free wind stream with the wind speed experienced by the rotor, by acting on the blade pitch angle or the generator torque of the upstream turbine, consequently affecting the amount of power extracted by it. This process, known as derating, reduces the turbine's power production, leading to an increase in wake velocity and recovery, which helps mitigate its impact on downstream turbines. [15]
Numerical simulations have shown that SIC's effectiveness is highly dependent on several factors such as wind farm characteristic design and layout and main atmospheric conditions. Studies suggest however that power gains from SIC are modest (few % points), with results indicating only slight increases in efficiency and also wind tunnel experiments support these numbers.
Nevertheless, SIC presents potential for other applications, such as balancing load distribution to extend the operational lifespan of the turbines. Although early steady-state simulations offered promising results while more recent research and experiments have demonstrated that the full-scaled benefits of SIC are smaller than initially anticipated. [18]

### 2.2.4 Horizontal and Vertical Steering

The steering strategy is a control technique that involves intentionally misaligning the upstream turbine with respect to the wind flow. This misalignment triggers the deflection of its wake away from downstream turbines, achieved by yawing (horizontally) or tilting (vertically) the rotor, letting the upstream turbine operate in not-optimal conditions but allowing the downstream turbines to capture more energy, increasing the overall power production of the wind farm. This wake deflection also tempers the increased loads and turbulence that downstream turbines usually experience. The main factors that influence wake deflection are represented by downstream and transverse spacing, yaw or tilting angle, orography and ambient conditions. [6]
Horizontal deflection has shown significant promise. Simulations have foreseen global power increases of up to 5% while wind tunnel experiments have experienced gains up to 21% and full-scale tests reported gains between 7% and 13%. [19] [20] Siemens Gamesa became the first company to commercialize wake steering, achieving an annual power production increase of up to 1%. [21] Horizontal steering results therefore nowadays the most widely implemented technique, also due to its straightforward implementation. Clearly, the direction of the wake deflection depends on whether the turbine is yawed clockwise or counterclockwise, and the orientation follows the rotor alignment. [6]

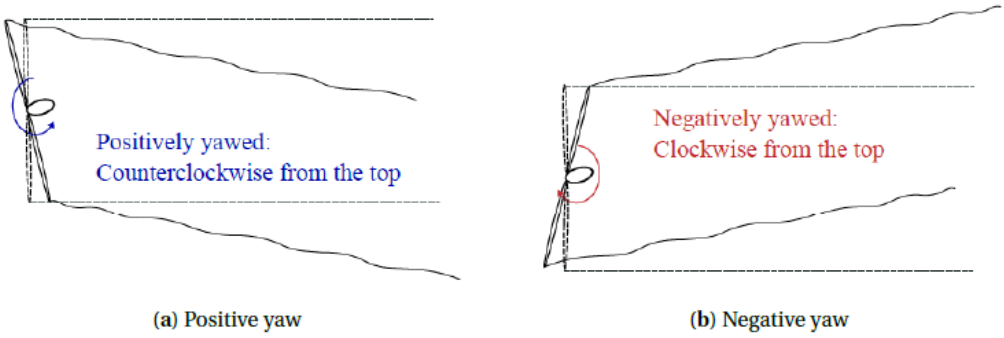


**Figure 2.7:** Horizontal wake steering [22]

Also the vertical variant of wake deflection, or tilt control, has gained ample interest. In this strategy, the turbine is tilted either upward or downward to deflect the wake vertically: downward wake deflection diverts the wake towards the ground, while upward deflection bends it towards the sky. This technique results particularly suited for offshore wind turbines on floating platforms equipped with active ballast systems, which allow accurate tilt adjustments. Regarding onshore turbines, this technique can be implemented instead of using fluid power platforms, but due to the higher investment costs and manageability issues, this makes it less worthwhile for onshore applications. [23]

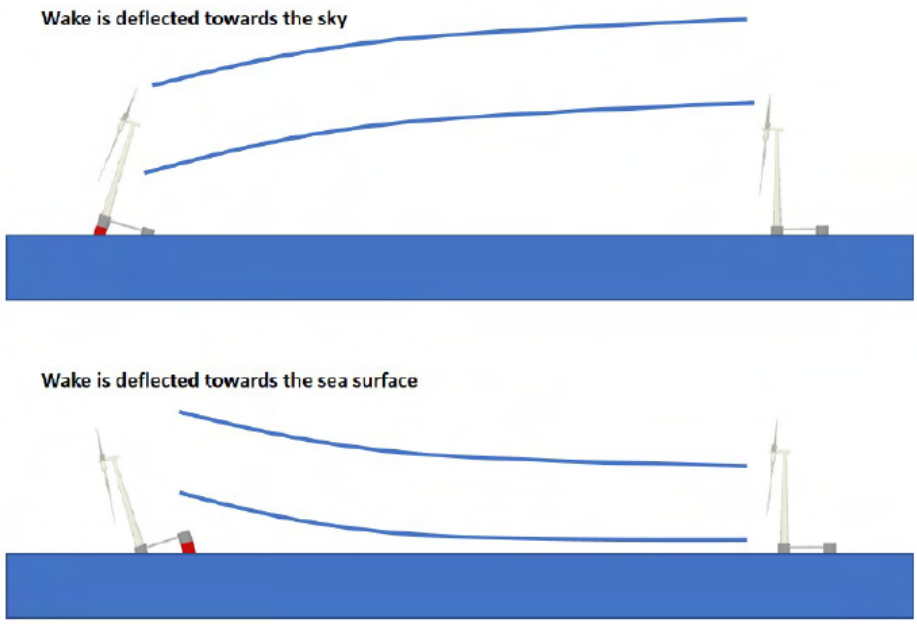


**Figure 2.8:** Vertical wake steering [23]

Preliminary simulations involving this control technique predict power gains between 8% and 13%, while in wind tunnel tests, the power gains observed with only two turbines amounted to 16.5%. However, wake recovery tends to occur faster with downward deflection due to faster turbulent mixing in the upper portion of the wake. Despite this, further research is needed to assess the loads on turbine structures and the costs involved, particularly for onshore applications. [23] [24]

### 2.2.5 Dynamic Induction Control

Dynamic control strategies, or active wake control, represent one of the most relevant research topics in the wind energy field, consisting of operating turbines dynamically to induce higher wake mixing and promote its faster recovery. [15] The characterisation of these techniques is realized through an adimensional factor called Strouhal number St, which compares the frequency of different-sized objects. Regarding wind turbines, it considers the control actuation frequency f, normalized with the rotor diameter D and the wind velocity U. [25]

$$S_t = \frac{fD}{U} \tag{2.11}$$

Dynamic Induction Control (DIC) is an advanced wind turbine control technology that aims to optimise global power production in wind farms by altering the induction factor over time through pitch control of the turbine blades. By sinusoidally adjusting simultaneously the pitch of all three blades, DIC generates a turbulent wind flow that creates a peculiar pressure wave, as a "pulse", that enhances wake recovery and improves the efficiency of downstream turbines to boost the overall wind farm power extraction capacity. Unfortunately, this technique not only increases global energy productivity but also introduces higher structural loads on turbines. [26]

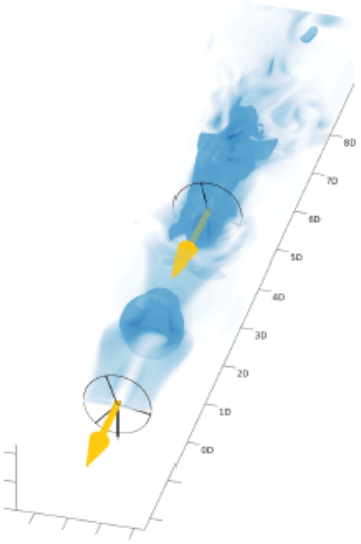

**Figure 2.9:** Wake pulse generation through DIC [15]

Large Eddy Simulations (LES) and wind tunnel tests have demonstrated significant power gains using DIC. Numerical evaluations have foreseen that coordinated DIC control can generate power increases ranging from 8% to 21% at an optimal Strouhal number of 0.25. Wind tunnel experiments, instead, experienced power gains of 2.4% in low turbulence conditions and up to 4% in high turbulence ones with St=0.3, proving the potential of the DIC technique to enhance wind farm efficiency. This experimental data was later also confirmed through LES-Actuator Line Method simulations, although registering a huge rise in fatigue loading on the turbines that reduces drastically the payoff of this strategy, making the DIC very suitable only for low and medium turbulence conditions. [27] [26]

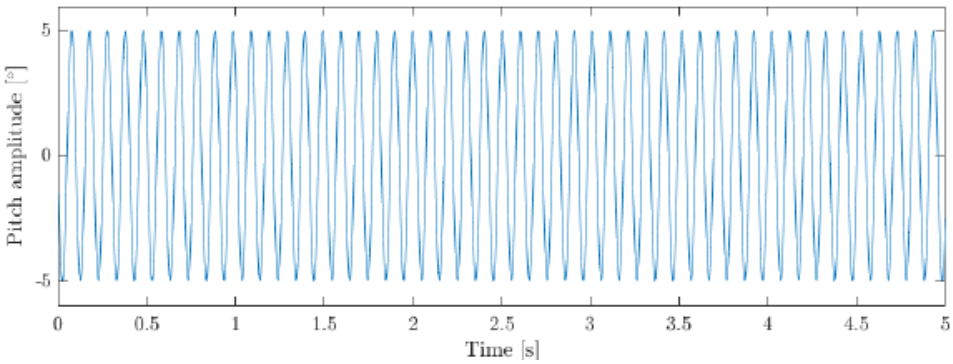


**Figure 2.10:** Input signal example for dynamic induction control [28]

Further studies and current research are investigating new variants of this control approach, such as a collective motion (PCM) of the blade pitch using Gaussian control or combining the DIC with wake steering and dynamic yaw controls. [29] [30]

### 2.2.6 Helix and DIPC

The Dynamic Individual Pitch Control (DIPC), also known as the "Helix" approach, is the most innovative control strategy in the wind energy panorama and it has drawn significant attention in recent research to enhance wind farm efficiency. Initially proposed by Frederik et al. [31], DIPC diverges from the DIC by altering the wake direction rather than acting on the induction coefficient to induce vortex breakdown. The root principle of DIPC involves adjusting individually each blade to alter its own pitch angle to generate tilt and yaw moments, which slowly drive the wake as it develops downstream. This directional control creates a helical-shaped wake (from this, the name of the theory), allowing for both vertical and horizontal movements of the wake during its expansion, resulting in a helical evolution confined into a conical shape. This rotational wake, or "Helix," enhances wake mixing and accelerates wake recovery, leading to significant improvements in global turbine performances.[32] [33]

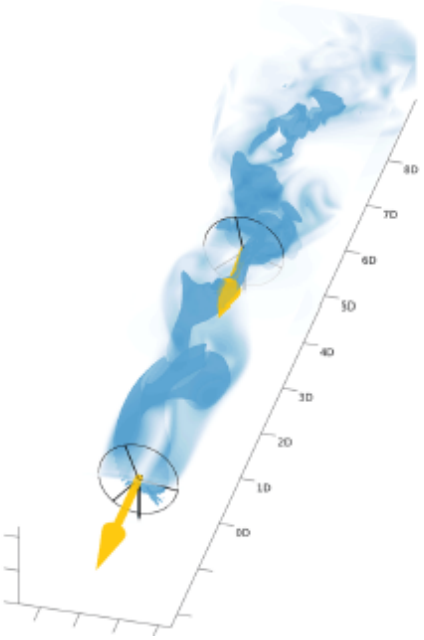

**Figure 2.11:** Wake helix [15]

The technical implementation of DIPC consists of the pitch-independent control of each turbine blade using sinusoidal excitation frequency defined as

$$f_\beta = f_r \pm f_e, \tag{2.12}$$

where $f_r = \frac{\omega_r}{60}$ is the rotational frequency of the rotor and $f_e$ is the additional excitation frequency. This modulation generates two variants of the same phenomenon, depending on whether the pitch control frequency is added or subtracted or on the phase relationship between these frequencies. In particular, if $\frac{f_\beta}{f_r} < 1$ the additional rotational motion occurs in the same direction as the rotor one leading to a clockwise (CW) helix development, while with $\frac{f_\beta}{f_r} > 1$ the wake meandering occurs in the opposite direction of the rotor one, so counterclockwise (CCW). [33]

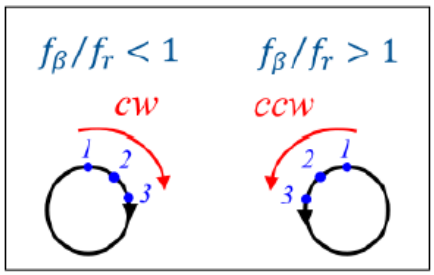


**Figure 2.12:** Helix directions explanation [33]

It must be added that the three blades are actuated individually by control frequencies shifted among them by a phase of 120°, as illustrated in Figure 2.13.

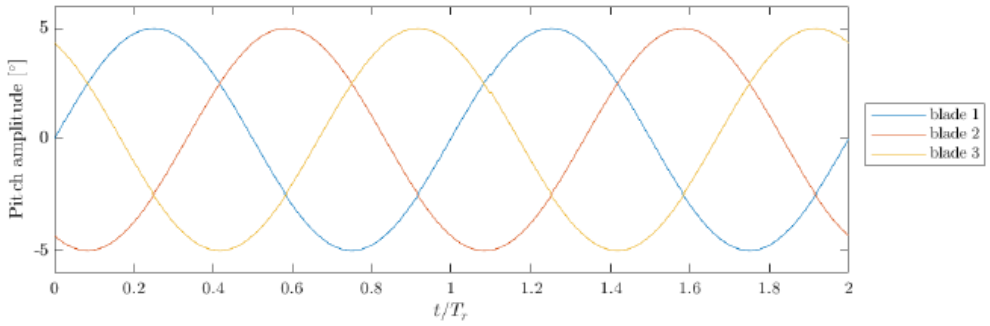


**Figure 2.13:** Input signal example for dynamic individual pitch control [28]

Recent research has investigated this symmetrical behaviour concerning actuation frequencies to find the optimal actuation spots in the control signal spectrum. Mühle et al. [33], using the same G1 turbine models in LWE at TUM operated in this thesis work, detect two symmetrical peaks in the actuation frequencies graph:

$$\left(\frac{f_\beta}{f_r}\right)_{\text{CW}} = 0.82 \quad \text{and} \quad \left(\frac{f_\beta}{f_r}\right)_{\text{CCW}} = 1.18 \quad \text{at} \quad \text{St} = 0.45$$

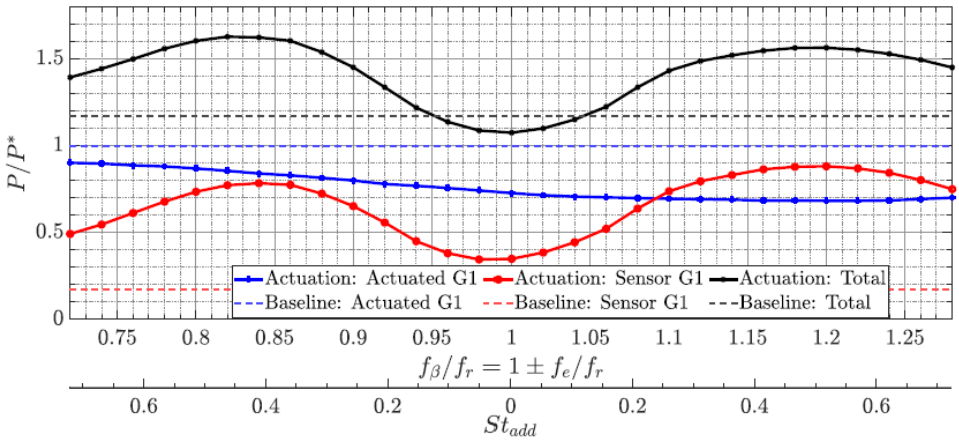


**Figure 2.14:** power peak individuation for DIPC control with G1[33]

The plot shows that the CW peak presents slightly higher overall power gains, with the upstream turbine performing better than the downstream one, while in the CCW peak, the behaviours are reversed. In the second case indeed, a faster wake mixing and recovery is achieved since the downstream turbine performs decisively better, experiencing however higher loads compared to the Helix 0.82 case. These differences derive from the different rotational direction of the Helix additional excitation and the different behaviour of the velocity components (u, v and w). The w component, in particular, can either act in the same (Helix 0.82) or in the opposite (Helix 1.18) direction of the wake rotation and therefore promotes better wake mixing for the Helix 1.18 case compared to the Helix 0.82 one. Due to these considerations and even though the wake mixing is stronger for Helix 1.18, the Helix 0.82 case results more preferable considering that the power gains of the two different actuation settings are almost identical but the loads and duty cycles of the CW case lead to a longer components life.[33]
Considering that the Helix approach is still relatively new, only preliminary results and studies are available in the literature. Firstly, Frederik et al. reported a 7.5% increase in power production [31] through numerical simulations, while other LES results have demonstrated power production gains of up to 12%, showing the potential of this technique. [32] Additionally, recent wind tunnel tests showed that a two-turbine setup using the Helix technique is able to experience power gains of around 15% [34] and till to an astonishing 40% obtained by Mühle et al. [33], although in very peculiar and favourable conditions.

In summary, DIPC and its Helix approach represent a significant perspective in wind turbine control, offering a promising solution for wind farm layout, and increasing power production while managing structural loads more effectively than the DIC methods. However, further research and studies have to be conducted to have a more complete understanding of how the helix wake would behave in real scenarios due to the complex aerodynamic phenomena that occur in the atmospheric boundary layers and moreover evaluate the practical feasibility of implementing such a peculiar dynamic control on full-scale models. [33]

### 2.2.7 Dynamic Yaw Control

This technique involves a dynamic adjustment of the yaw angle of a turbine to actively mix the wake behind the turbine and promote a faster recovery. The yaw is constantly modified with a sinusoidal pattern, letting the rotor oscillate around the main flux direction to meander the wake (lateral oscillatory motion) and to obtain a lower impact on the downstream turbine. [15]

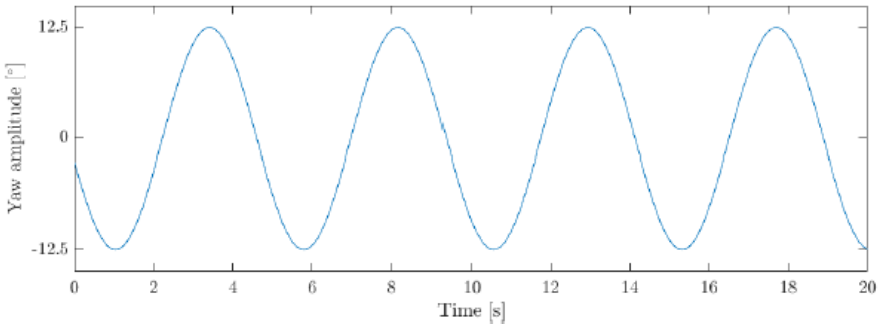


**Figure 2.15:** Input signal example for dynamic yaw control [28]

LES simulations conducted in the most recent studies about this control technique show that the benefits reached are even slightly lower with respect to the static steering approach, with a 4.6% overall power gain for dynamic and a 5.3% for the static yaw case for a six-turbine array under neutral atmospheric boundary conditions. Following research and wind tunnel experiments experienced good results and a further understanding of how the wake meandering and technique efficiency depend on the optimal operating St numbers, on the amplitude of the oscillations and on the turbulence conditions. [35]
The amplitude results in a more impacting factor with respect to the actuation frequency, even if the most suitable operating values for these two parameters lie beyond the full-scale yaw actuation system operating limits and therefore a trade-off is necessary to ensure practical feasibility. Moreover, it is demonstrated that in high-turbulence scenarios, the technique did not show any benefits since the

natural wake mixing results already triggered by boundary layer turbulences and phenomena. The application of this technique, therefore, would only be considered for special wind farm layouts with low Ti conditions, with low prospectives regarding real-case scenarios. [15] [36]

### 2.2.8 New frontiers and combined control techniques

The present challenges in the wind energy sector regard today the combination of more than one control technique at the same time, to understand if further power gains can be achieved. Recent wind tunnel experiments performed here in the LWE at TUM University showed, for instance, how the combined horizontal and vertical steering could lead to interesting profits, with gains higher with respect to the single techniques actuated alone. Another interesting prospect was represented by the implementation of dynamic pitch controls on the wake steering. Unfortunately, preliminary results showed no gains with respect to the DIPC actuated alone since the Helix seems to hinder the effects of the wake deflection, even if further tests with greater distances between the turbines have to be explored.[28]
However, the research path results still long and many issues must be addressed, such as the practical implementation and feasibility of the more complex dynamic control techniques on real-scale turbines. [29]

# Chapter 3

# MULTI-PROBE SENSOR DATA ANALYSIS

## 3.1 Introduction and probe description

### 3.1.1 Multi-probe sensor devices

Multi-hole probes are specialized instruments used in fluid dynamics and aerodynamic applications to measure the velocity and direction of fluid flow accurately. These probes are essential for the understanding of the complex flow fields around objects, particularly in wind tunnels or in real-world scenarios like aircraft testing or wind turbines. [37]

A multi-hole probe typically consists of a head with multiple holes connected to pressure transducers able to detect the pressure at each hole location. Thanks to these multiple simultaneous measurements and its distribution around the probe, the probe is capable of capturing different measuring variables as:

- Total and static pressure
- Angle of attack (AoA) of the flow
- Flow velocity
- Related thermodynamic properties

The arrangement and number of holes can vary and depend on the application and required precision. The design of the probe tip and the number of holes on the probe's head are tailored to meet the measurement needs. Down here are listed for example all types of probes produced by Vectoflow:

- **1-hole probes** (Prandtl or Kiel) can measure dynamic and total pressure.
- **3-hole probes** are used for 2D measurements, such as within boundary layers and can detect flow speed and direction (AoA).
- **5-hole probes** are suitable for measuring flow angles up to 60°.
- **7-hole probes** can handle flow angles up to 70°.
- **14-hole probes** are designed for measuring reverse and more complex flows.

Concerning probes up to 250 mm, they are typically crafted from a single piece using additive manufacturing, with all necessary functions integrated into the design, resulting in a highly durable product. These probes are commonly made from materials like grade 5 titanium, Inconel, and stainless steel while larger ones instead usually feature an additively manufactured head with extension parts to achieve the higher complexity required. The tips and reference surfaces are precisely machined for optimal aerodynamic accuracy and performance, moreover, the required pressure tubes are attached using adhesives, brazing, or laser welding, depending on the specific application. Mechanical analysis of the probes can be conducted through 1D calculations or Finite Element Method (FEM) analysis upon request. [37]

The principal application fields of such probes are wind tunnel testing to map the flow around models, aerospace engineering for testing and improving the aerodynamic performance of aircraft, spacecraft and other vehicles, turbomachinery analysis to understand the flow within rotating machinery and environmental monitoring to study atmospheric flows, such as wind patterns over complex terrains.

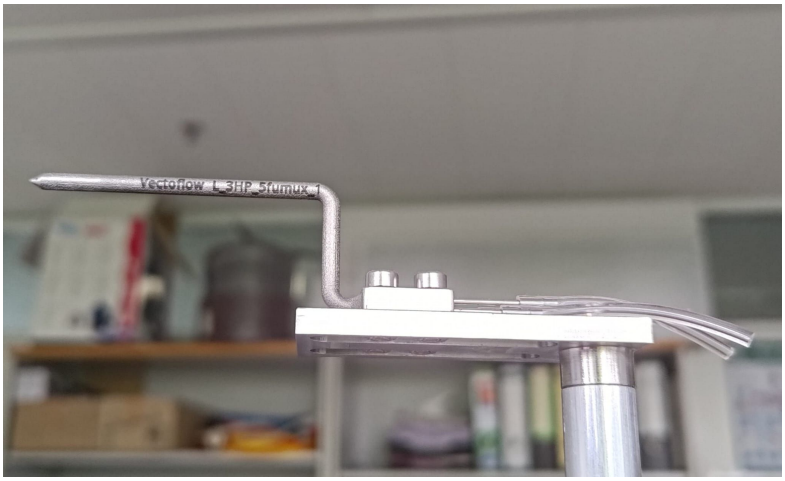

**Figure 3.1:** 3-hole probe in the Chair

A 3-hole probe has been acquired by the Wind Energy Chair (LWE), and shown in Figure 3.1, with the purpose of substituting Pitot tubes and being installed on all the turbine models since it is able to detect not only the wind speed with a higher accuracy level but also his direction with respect to the turbine rotor axis orientation. This allows therefore to integrate a Pitot tube with a wind vane in a unique electronic measuring device. It is therefore capable of providing highly accurate measurements of both velocity magnitude and direction in various flow conditions, including subsonic, transonic, and supersonic flows also with a 3D mapping. Naturally, it must undergo careful calibration to ensure accuracy, especially in non-uniform or turbulent flows, and complex data processing and interpretation with sophisticated algorithms and software are required.
The following sections briefly describe the characteristics and functions of the "obsolete" devices mentioned above, such as the Pitot tube and the wind vane.

### 3.1.2 Pitot tube

A Pitot tube is a measurement device able to detect the speed of a fluid flow. It consists of a tube with an open end pointing directly into the fluid flow and is able to capture the pressure caused by the fluid's velocity. This device is the most commonly used in all the principal applications concerning air flows, such as aviation or wind energy to measure for example the airspeed of an aircraft and in other various engineering applications to measure fluid flows in pipes and channels. [38]

The function is extremely simple and is based on Bernoulli's equation (derived from the energy conservation principle), which is applied to a horizontal flow case.

$$P_s + \frac{1}{2}\rho v^2 + \rho g h = P_t \tag{3.1}$$

where:

- $P_t$ is the total or stagnation pressure,
- $P_s$ is the static pressure,
- $\rho$ is the fluid density and $v$ the fluid speed
- $\frac{1}{2}\rho v^2$ is also defined as dynamic pressure

**Figure 3.2:** example of a Pitot tube [39]

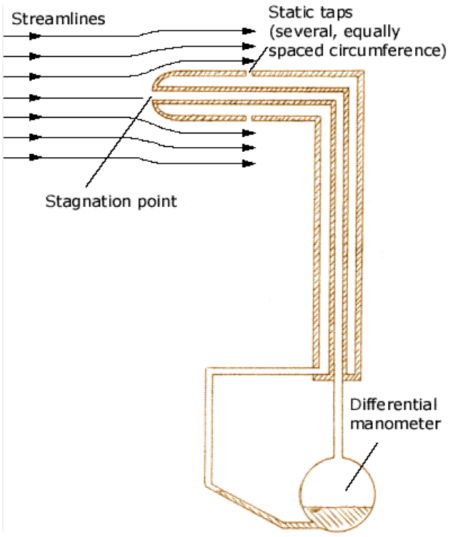


**Figure 3.3:** Pitot tube section[40]

The working principle of a Pitot tube can be therefore briefly summarized as:

1. **Positioning:** The open end of the tube placed in the flow and facing directly in it is known as the **stagnation point**, or the point in which the fluid flows stops and has its maximum static pressure equal to the total pressure since all the dynamic one vanishes with the velocity.

2. **Pressures measurement:** The principal tube measures therefore the total pressure while a second tube positioned usually around the other one is able to detect the static pressure of the fluid, which is the pressure exerted by it in all directions due to the random molecules motion.

3. **Dynamic pressure evaluation:** Thanks to a differential manometer usually, the difference between the total and the static pressure can be evaluated and this results equal to the dynamic one. Thanks to the inverse of the Equation 3.1, it is possible to achieve the actual fluid flow speed as: [38]

$$v = \sqrt{\frac{2(P_t - P_s)}{\rho}} \tag{3.2}$$

As specified above, Pitot tubes are the most adopted devices concerning airflow speed measurements due to their simple design but with accurate measurements and the absence of moving parts, making them durable and low-maintenance. Their use is extremely wide in a huge number of different applications even if their accuracy

can be affected by turbulence and misalignment with the flow. They also turn out to be unsuitable for both low-speed measurements due to the small pressure differences and for very high-speed ones since they would require correction factors to take into account flow compressibility. [38]

### 3.1.3 Wind vane

For what concerns instead the wind direction identification, the traditional and most widely instrument adopted is the wind vane. Essentially, it consists of an asymmetrical slender body mounted on a vertical axis, able to rotate freely around it. The vane is designed with a broad tail on the downwind side and a counterweight on the upwind one to provide balance at the rotating hinge. When the wind exerts a force on the vane, it causes it to align with its direction, with the end that provides the greatest resistance pointing downwind or leeward.[10] [41]

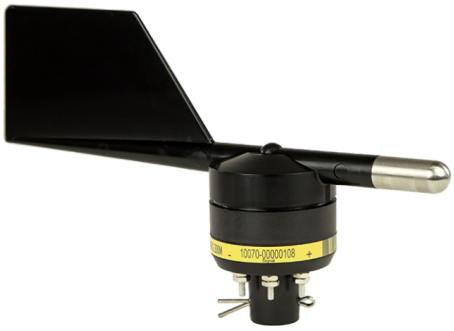

**Figure 3.4:** Example of a modern wind vane by NGR Systems. [42]

One of the most problematic issues results in the presence of a starting threshold, or a minimum wind speed that the vane must undergo to start movement. This threshold typically ranges between 0.5 and 1 m/s, making this "ancient" instrument not suitable for precise low-speed application. Moreover, the motion of the vane must be damped to prevent rapid and wrong changes in direction due to sudden turbulence or disturbances. Wind vanes typically generate analogue signals either through contact closures or potentiometers that are converted into digital signals by a transducer in modern devices. [10] [41]

## 3.2 Data acquisition and post-processing

In the previous months, several wind tunnel tests (in the Wind Channel number 3) have been performed in the department with the new probe in order to compare his measurements with the ones achieved by a classic Pitot tube, and to understand the reliability and the accuracy of the new device. Several wind speeds and directions have been investigated to have a complete overview of the probe characteristics. During the wind channel campaign, the probe and the Pitot have been located at some height and at a horizontal distance of circa 30 cm in the middle of the channel section to guarantee the most homogeneous and equal flow possible. All the data acquired were then post-processed using a special and complex Matlab script supplied directly by the Vectoflow company in order to obtain the speeds and orientations of the various tests starting from the pressures acquired during them.

The data have been collected and plotted in graphs illustrated in the next sections. Interpolated lines have been created through the Matlab function "polyfit" which uses first-degree polynomials to achieve such functions in order to observe the measured data dispersion from the ideal values.

Moreover, for what concerns the velocity observations, a dimensionless coefficient of the velocity fluctuations relevance compared to the mean velocity has been investigated. Such a measure is called Turbulence Intensity (Ti) and it is expressed by the following formula:

$$Ti = \frac{\sigma_u}{\overline{u}} \times 100\% \tag{3.3}$$

where

- $\sigma_u$ is the **standard deviation** of the velocity fluctuations (which measures the spread or variability of the instantaneous velocity around the mean one).

- $\overline{u}$ is the **mean velocity** of the flow.

This ratio provides so a dimensionless measure of how significant the velocity fluctuations are compared to the mean velocity; it is then multiplied by 100% to convert it into a percentage, which is how Ti is typically expressed. [10]

## 3.3 Results evaluation

### 3.3.1 Wind velocities investigation

The first plots present the comparison between the wind velocities captured simultaneously by the multi-hole probe and the Pitot tube at different angle orientations described by the angle $\gamma$. The positive and negative values of $\gamma$ have been adopted to distinguish the left or right directions.

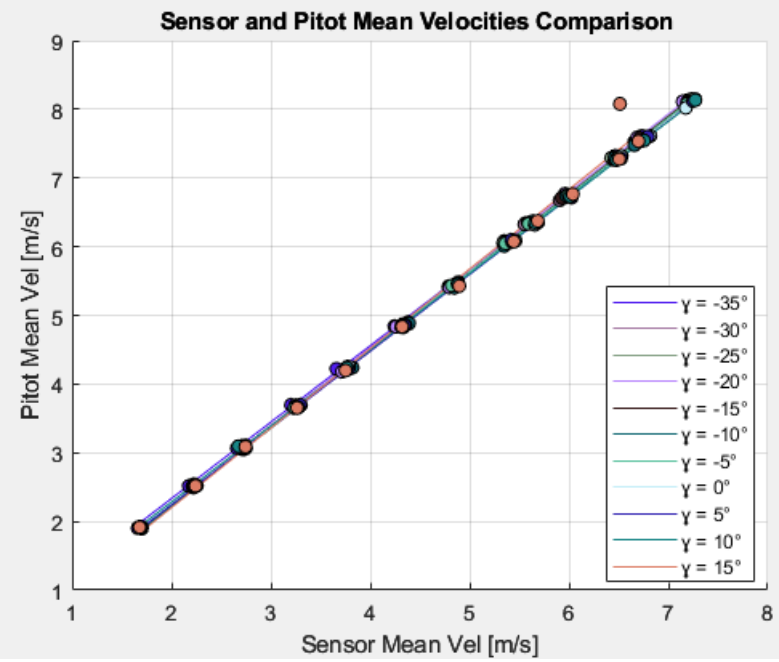


**Figure 3.5:** Pitot and probe velocities

As depicted in Figure 3.5, the probe tends to slightly underestimate the velocity values with respect to the Pitot despite the measurements remaining homogeneous with all the orientations. The outcomes can be therefore considered mostly satisfying as also confirmed by the plots in Figure 3.6 and 3.7, where the interpolating coefficients and the residuals (difference between the actual value and the interpolated ideal one) are plotted for the various wind orientations.

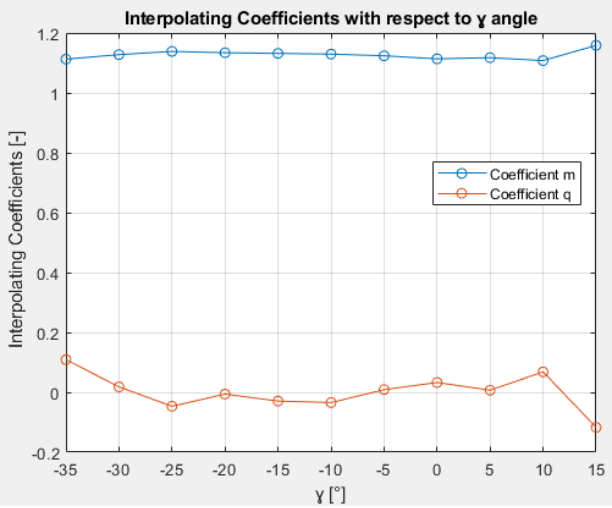


**Figure 3.6:** Velocity interpolating coefficients

The coefficients of the interpolating lines have been resulted extremely coherent among them, describing functions close to

$$y = x \tag{3.4}$$

that would be the ideal result. Indeed m coefficients result close to 1 and q close to 0, considering that a first-degree polynomial is described by

$$y = mx + q \tag{3.5}$$

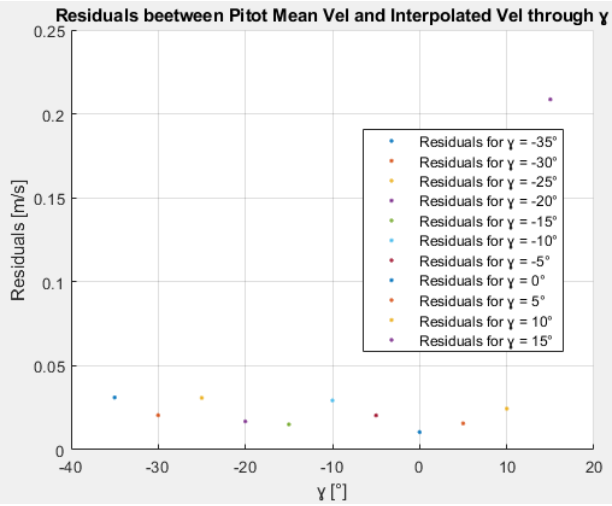


**Figure 3.7:** Velocity residuals

The residuals lay, indeed, all under a value of 0.25, which is a great result in terms of accuracy and consistency.

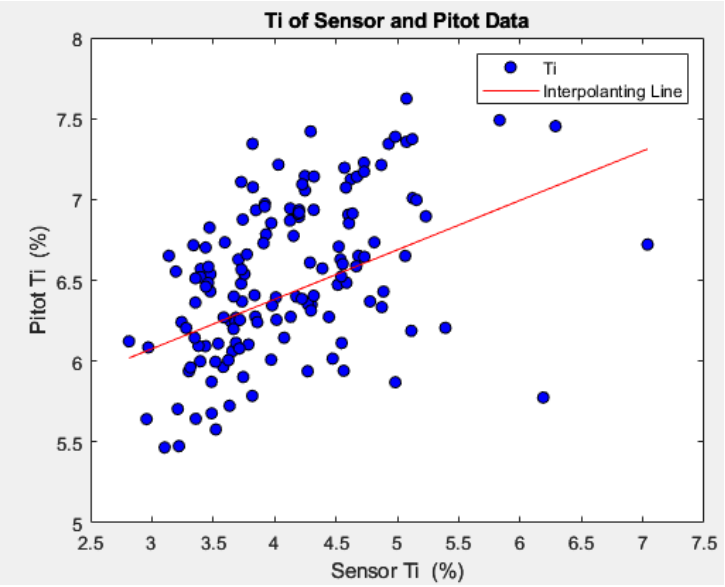


**Figure 3.8:** Velocity Ti

Lastly, the Ti values are illustrated in Figure 3.8. They show how the multi-hole probe seems to be less influenced by the velocity fluctuations reaching lower Ti values with respect to the Pitot tube. This represents a great improvement that the probe can guarantee if it would be used instead of the tube.

### 3.3.2 Wind directions investigation

Instead, the following plots illustrated the wind directions detected by the sensor at different wind velocities compared with the actual orientations in which the Pitot has been positioned during the measurements. Of course, to achieve different wind directions, the probe has been rotated with respect to the main flow direction in the channel and not the opposite.

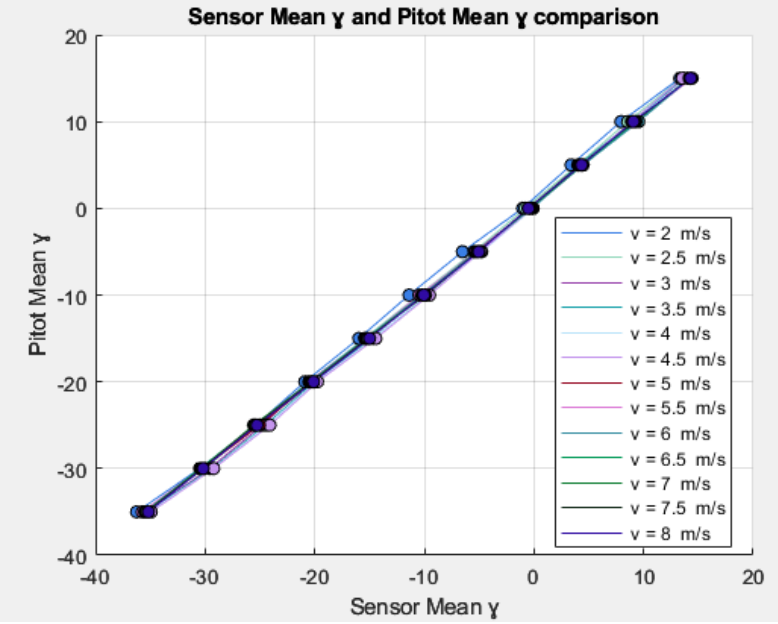


**Figure 3.9:** Wind direction detected by the probe

As depicted in Figure 3.9, the wind directions measured by the probe are genuinely accurate with respect to the actual ones with interpolating lines extremely close to the ideal sector bisector.

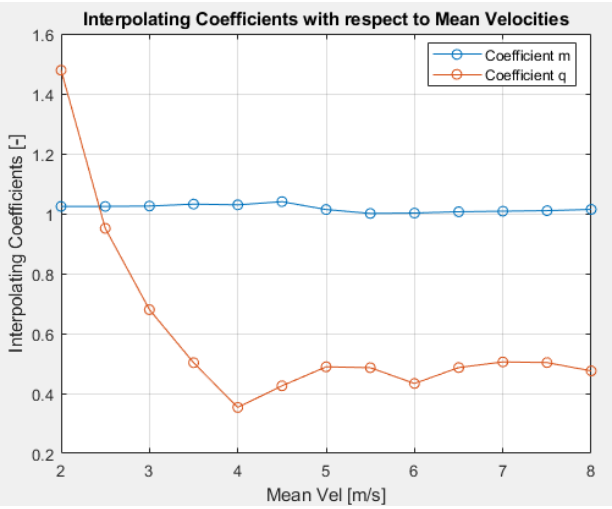


**Figure 3.10:** Angle interpolating coefficients

The interpolating coefficients indeed exhibit a reasonable consistency (especially m), except for the low-speed values, which may be caused by the low homogeneity of the low-speed airflow in the channel or, more likely, by accidental measurement errors.

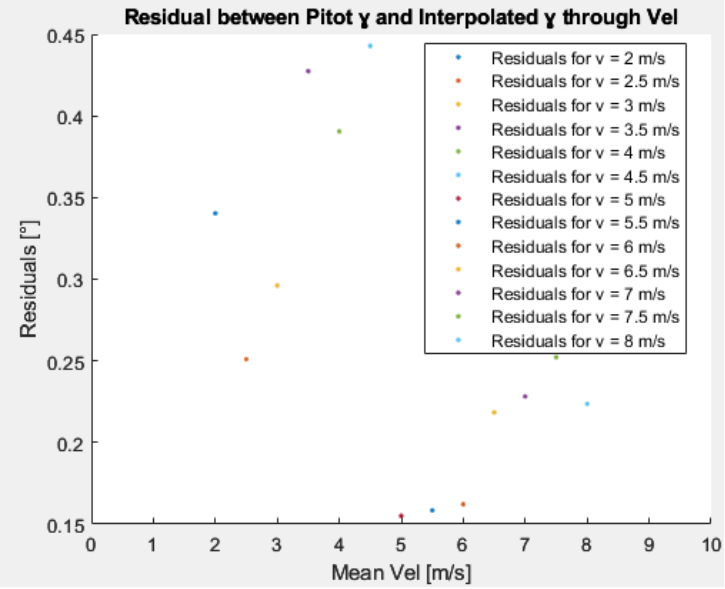


**Figure 3.11:** Wind direction detected by the probe

Lastly, the residuals of the angle measurements are illustrated in Figure 3.11. They are larger in terms of absolute value with respect to the ones obtained for the velocity but, since the angle range is wider compared to the speed one (from -35° to 15° with respect to from 2 m/s to 8 m/s), in percentage terms their impact is widely lower even if larger.

### 3.3.3 Conclusions

The results obtained and discussed above confirm that the implementation of a multi-hole probe could be a great improvement for the turbine models used in the Chair (and it will be done in the next months), in order to have a more accurate, modern and directly integrated sensor extremely useful especially for the yaw control.

# Chapter 4

# G1 TURBINE MODEL

## 4.1 Technical description and characteristics

The G1 wind turbine model represents the most relevant and used machine in the Wind Energy Department (LWE) at TUM due to its compact dimensions combined with plenty of controls and sensors available.

The G1 wind turbine model is a scaled-down version of a full-sized turbine, specifically the DTU 10 MW wind turbine [9], carefully crafted to investigate and comprehend the dynamics of wind energy conversion. It is equipped with a rotor spanning approximately 1.1 m in diameter and a tower 0.8 meters tall, this model is able to adeptly incorporate the key features of a full-scale wind turbine. It provides a controlled setting for in-depth experimentation, allowing for a detailed study of wind energy systems. The turbine is well illustrated in Figure 4.2 and its main mechanical characteristics are presented in the table contained in Figure 4.1. [43][44]

| | |
|---|---|
| No. of blades | 3 |
| Rotation | Clockwise |
| Rotor diameter $[m]$ | 1.1 |
| Hub height $[m]$ | 0.83 |
| Rated rotor speed $[rpm]$ | 850 |
| Rated power $[W]$ | 46 |
| Active yaw control | yes |
| Active pitch control | individual |

**Figure 4.1:** G1 wind turbine mechanical characteristics [43][44]

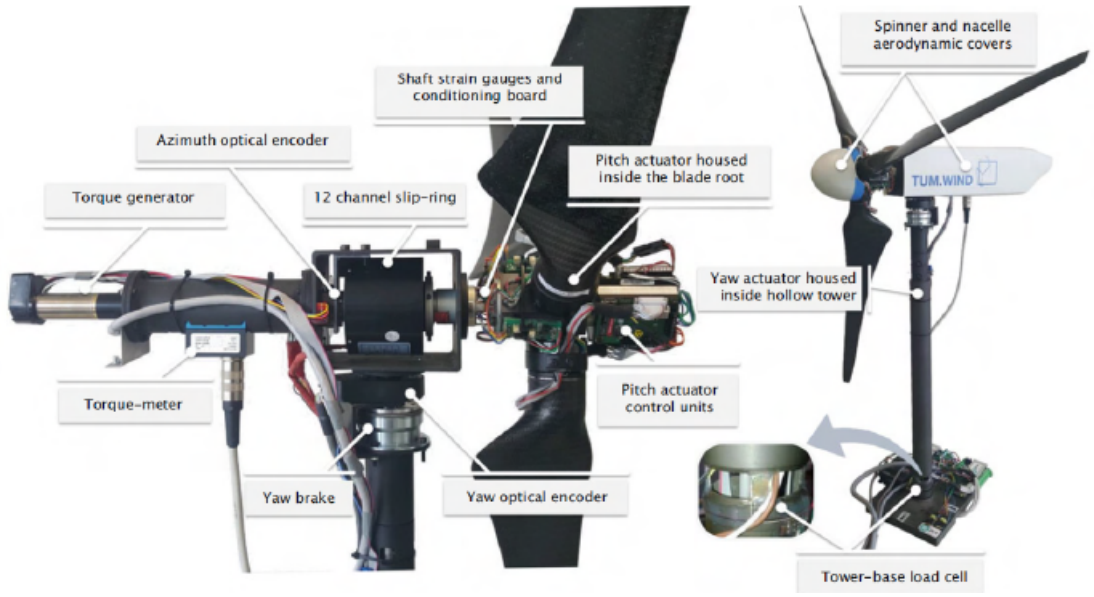


**Figure 4.2:** G1 wind turbine [43]

The model's key hardware components include a set of motors and generators to drive the rotor shaft or convert its rotation into electrical power, control the yaw rotor orientation and adjust the pitch of each blade. These motors are the model's core, managing the turbine's various operational aspects.
The nacelle, or the main turbine part, is crucial for linking the model's mechanical and electrical systems and represents the connection point between the rotor and the turbine structure. Starting from the front, a hub is present with the 3 pitch control boards directly connected to each blade motor (one board controls and manages one blade) and to a Hall sensor, used to detect the actual pitch angle of each blade. This allows one of the most relevant features of this turbine model: the individual pitch control or IPC. In synthesis, each carbon fiber blade can be twisted individually to modify its $\beta$ angle and therefore is AoA during the operation modifying the power extraction capacity, the rotor efficiency and balancing and the loads acting on the turbine structure. [33] Following the shaft, the blades are connected in the proper housings with their pitch actuators and hall sensors as described above. Then the shaft strain gauges and their proper conditioning boards are located to detect the forces and moments acting on the shaft. All these components are mechanically and electrically connected to a special metal hollow case in which is located the slip ring. This is a particular component that allows the transmission of electrical signals between rotating and fixed cables through brushes. Behind it, the azimuth optical encoder is then located to read the shaft rotations and to locate the actual azimuth position during the operations. The whole rear block linked to the nacelle cis contained instead in a huge cylinder hollow case, connected

through fastened flanges, that hosts the continuation of the shaft, a torque meter and lastly the rotor actuator, able to perform as a motor or as a generator. It must be specified that all these components are connected through mechanical flexible joints to permit slightly relative axis movements or misalignments. Moreover, the metal hollow case is mechanically linked to the yaw actuation system on the tower and is capable of rotating. This system consists of an actuator, a magnetic disk brake and an optical encoder for the yaw position detection. The tower is hollow and is housed in the turbine basis with other strain gauges for the tower load detection. Additionally, electronic boards, each dedicated to a specific motor, are positioned in such a basis and provide the necessary control, converting commands into physical actions for synchronized operation or conditioning (for example the strain gauge output electric signals need to be amplified to be managed by the acquisition system). [43][44]

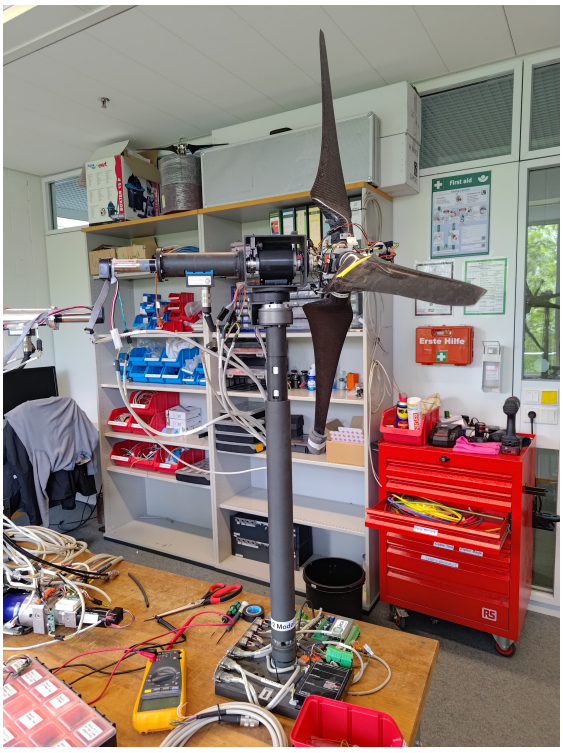


**Figure 4.3:** G1 wind turbine overview

The whole batch of control and conditioning boards located on the turbine structure or basis communicate with a specialized cabinet via a CAN (Controller Area Network) communication system. Such a cabinet houses a Bachmann M1 PLC control system that serves as the central hub for both power supply and control

and is illustrated in Figure 4.4. Data from encoders, along with any analogic or digital input/output signals, are directly routed from the motors to their respective electronic boards and converge into their specific Bachmann modules located in the cabinet. The core of this control system is represented by the CPU of the Bachmann system, which commands and orchestrates turbine operations, whether executed automatically or under manual control. Beyond its control functions, the cabinet is also equipped with digital capabilities, connected via Ethernet to interact with the "Solution Center" online interface. This software provides a graphical interface to have a real-time observation of the sensor outputs, perform the calibrations and practically control all the turbine functions, such as pitch, yaw and rotor control. Additionally, a USB interface within the cabinet stores essential turbine model information, including calibration files and matrices for sensors and specific motor data. This USB connection also functions as an external memory bank, capturing crucial test data during wind tunnel experiments and evaluations. It must be added that these control and connection protocols have been adopted by all the different turbine models used in the Chair. [8][43]

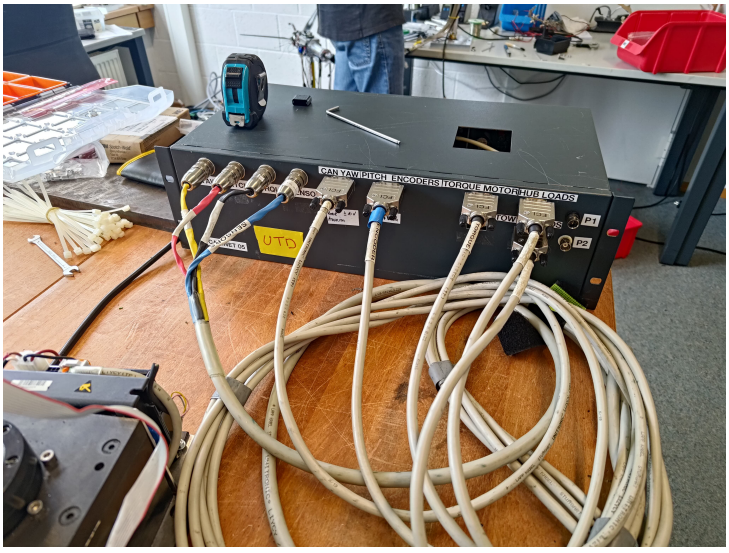


**Figure 4.4:** Bachmann cabinet with connections

This scaled wind turbine model, equipped with its specialized hardware, serves as a comprehensive platform for studying wind energy generation, static and dynamic control mechanisms and structural behaviours. It offers valuable insights into wind turbine dynamics, aiding in the advancement of renewable energy technology and sustainable power generation and testing and discovering new control strategies like the ones investigated in the last section of the chapter.

## 4.2 Preliminary operations and sensors calibrations

### 4.2.1 Maintenance and missing part assembly

Everything described below has been done for two G1 models, in particular the M1 and M2. The initial tasks concerning these models used in the Chair have been:

- a preliminary check of the models' global conditions
- substitution of the missing or damaged components (as mechanical joints or fastening items)
- a complete check of the wiring connection since many connectors were damaged or old, so it has been necessary to perform an almost global rewiring of the model connectors
- a sensor global check to guarantee their functioning during operations

After all these operations, the two G1 models were ready for the calibration procedures.

### 4.2.2 Calibration outline

Sensor calibration represents a meticulous and iterative process aimed at aligning a sensor's output with the actual physical quantity it measures. This involves a series of adjustments, fine-tuning, and systematic comparisons between sensor outputs and known reference values or standards (as loads applied or pitch positions), allowing for the quantification and rectification of the sensor's inherent errors, non-linearities, drifts, and offsets. Calibration enhances the sensor's reliability and accuracy, transforming raw electrical data into meaningful physical parameters.[45]

In the context of this project, the G1 wind turbine is equipped with many sensors: strain gauges on the hub shaft and at the tower basis for the loads, as well as Hall sensors on each blade for pitch control. The calibration of these sensors is crucial for the machine's operation, as the unique combination of assembled parts transmits varying signal strengths and magnitudes to each sensor. The aim of these processes is represented by the calibration matrices, obtained as explained in the following sections, to be inserted into the specific USB sticks of each model connected to the Bachmann during all the working operations and containing all the files and program codes referred to that specific model.

### 4.2.3 Blades calibration

For the Hall sensors, the blades' calibration ensures that electrical signals accurately correspond to the exact position of each blade in terms of $\beta$ angle. Regular calibrations are particularly important for the blades due to the wear and tear of the magnets.

The experimental setup involves securing one blade at a time with a vise, connected to the hub on a horizontal surface and powering the specific control board on it. A digital inclinometer, positioned on a specific template that precisely matches the blade's contour, has been used to measure the blade's pitch angle, as illustrated in Figure 4.5. The blade's motor, controlled by the specific proprietary software "Epos Studio" through the pitch control board has been operated in position control mode and retrieved analog output signals corresponding to the Hall sensor's voltage readings. The operation starting point has been achieved by an initial Homing procedure that consists of allowing to spin the pitch motor till a specific pitch position marked as the "home" or "zero" one and, starting from it, all the $\beta$ angles will be identified. These paragraphs describe the procedure for a single blade, but naturally, the same procedure has been applied to all the blades of the G1 models involved. [46]

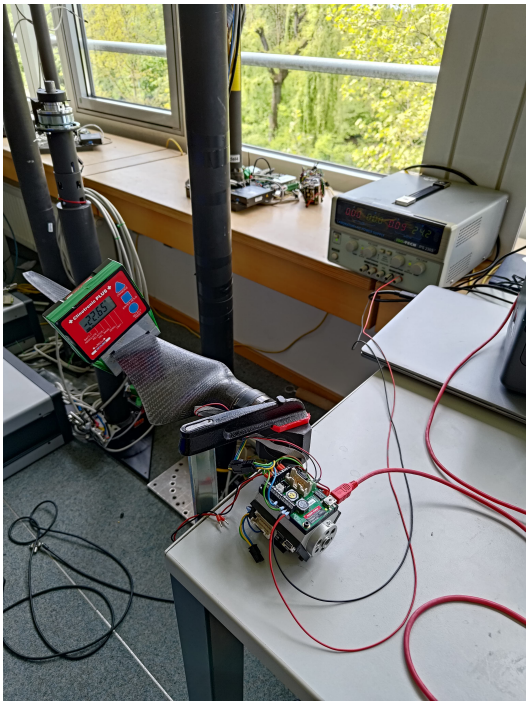

**Figure 4.5:** G1 blade calibration procedure

The calibration procedure has been involved in obtaining various Hall sensor outputs and the corresponding blade tilt angles exploiting multiple motor positions. These data have been employed to construct two curves: one showing the motor position values versus the blade tilt angles, and the other depicting the Hall sensor outputs versus the blade tilt angles. The Hall sensor fixed underneath the blade gears, as explained in the previous sections, is able to capture differences in the magnetic field generated by two magnets fixed to the gears rotating with the blades.

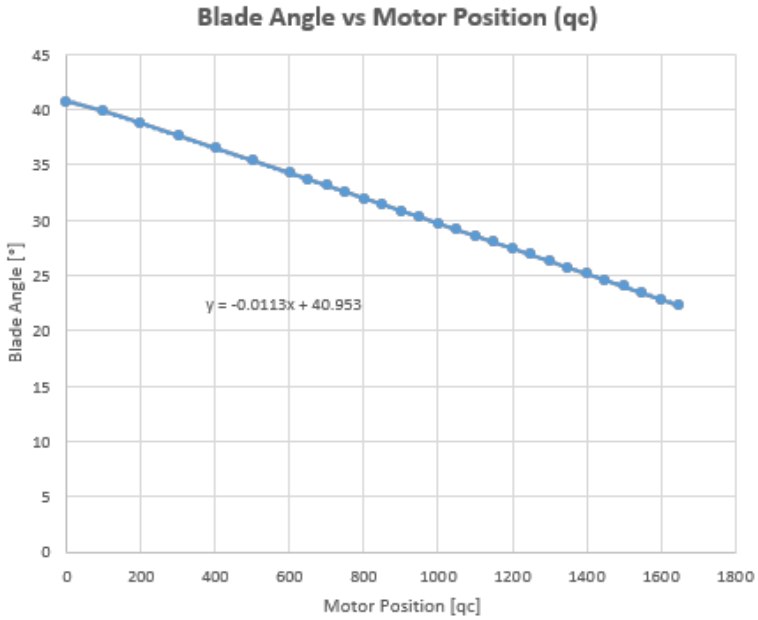


**Figure 4.6:** Pitch actuator relative position vs actual blade angle

In the first graph in Figure 4.6, a linear interpolation has been created between the pitch actuator's relative position and the blade angle. This relationship allows for the correlation of specific motor movements with the measured blade angle. The second graph in Figure 4.7 has been exploited instead to determine the initial pitch angle of the blade. Within the blade's motor assembly, a spring mechanism returns the blade to a position corresponding to approximately 2500 mV of the Hall sensor output when the turbine is not in operation. Accurately aligning the Hall sensor output with the blade tilt is essential to detect the exact initial pitch angle, which is critical for making adjustments during the model's operational phase.

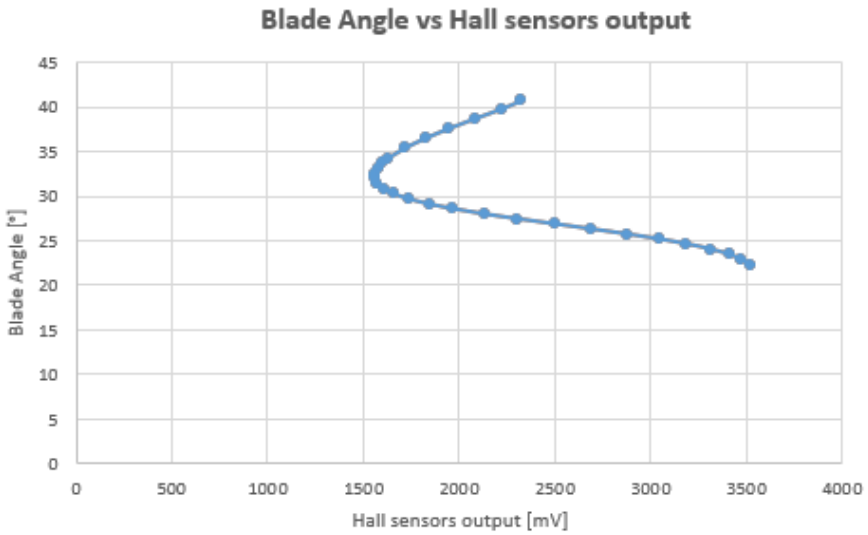


**Figure 4.7:** Actual blade angle vs Hall sensors output

### 4.2.4 Shaft or hub sensors calibration

Regarding the strain gauges, the goal of the calibration processes is to establish the relationship between the voltage signals and known loads, or moment forces, allowing for the estimation of torque and bending moments acting on the turbine. This involves applying weights of various magnitudes to generate moments and forces on the turbine components, with similar methods used for both the tower and the shaft, providing valuable insights into the stresses and strains experienced by the wind turbine model.

The hub calibration process examines three distinct types of moments (two bending moments and the torsion one): [8]

- **Side-Side (SS):** This refers to the force or moment causing the wind turbine to tilt or bend horizontally, perpendicular to the tower's axis.
- **Nodding or Fore-Aft(FA):** this involves the up-and-down tilting or nodding motion of the hub or blades, influenced by vertical forces such as wind speed variations or the weight of the components.
- **Torque:** This is the rotational force applied to the wind turbine rotor.

It must be specified that this convention of the bending moments has been adopted for all the turbine models in the department and it is summarized in Figure 4.8. The calibration matrix for the hub strain gauges is built in the following way:

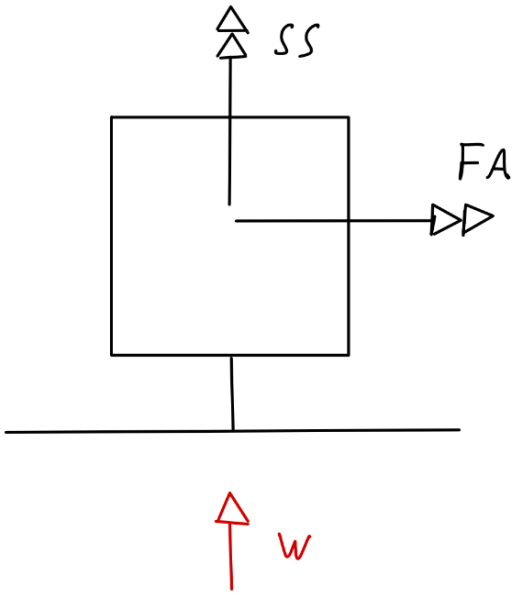


**Figure 4.8:** Adopted convention for bending moments

$$\begin{pmatrix} T \\ M_{\text{Fore-Aft}} \\ M_{\text{Side-Side}} \end{pmatrix} = \mathbf{C}_{\text{matrix}} \cdot \begin{pmatrix} V_T \\ V_{\text{Fore-Aft}} \\ V_{\text{Side-Side}} \end{pmatrix} \tag{4.1}$$

where $V_T$, $V_{\text{Fore-Aft}}$, and $V_{\text{Side-Side}}$ represent the voltage values read by the respective sensors for Torque, Fore-Aft and Side-Side moments measurements.

From this, as both the applied moments and the measured voltages are known, the shaft calibration matrix can be obtained as follows:

$$\mathbf{C}_{\text{matrix}} = \begin{pmatrix} V_T \\ V_{\text{Fore-Aft}} \\ V_{\text{Side-Side}} \end{pmatrix}^{-1} \cdot \begin{pmatrix} T \\ M_{\text{Fore-Aft}} \\ M_{\text{Side-Side}} \end{pmatrix} \tag{4.2}$$

Thanks to the calibration matrix, the control program are able to reconstruct the loads acting on the turbines during the working operations using the recorded voltages and subsequently calculate the errors incurred during the process. [46]

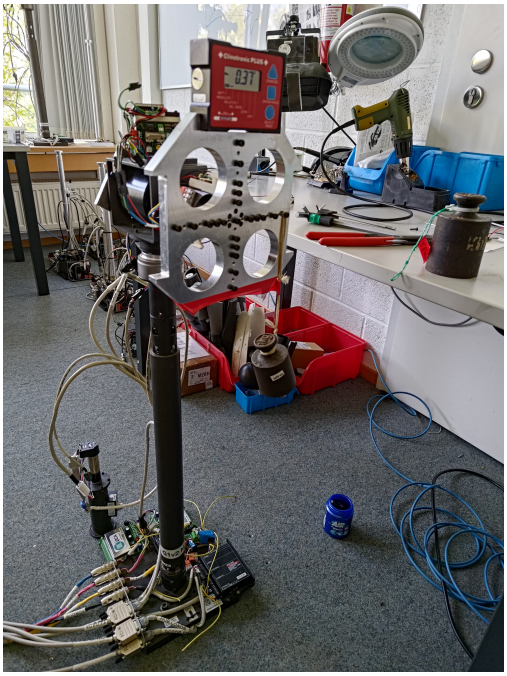

**Figure 4.9:** G1 shaft calibration procedure

The hub calibration procedure has been started disassembling the generator back batch and the hub with the pitch control boards from the front side. A specialized tool, consisting of a metal plate with protruding screws fastened in specific locations representing discrete axial distances, has been then fixed on the rotor axis to allow the weights to hang; the rotor axis has been also blocked with another small plate to inhibit unwanted rotations. Then, positioning the hub at the four key azimuth orientations (0°, 90°, 180° and 270°), different weights were suspended from the fixed locations on the plate with careful measurements of the axial distance. For each setup, the offsets have been removed before measuring and the inclination of the plate relative to the rotor's azimuthal orientation has been identified with an inclinometer located on the plate itself since it plays also a role in the moment calculation. [46]

The data obtained have been then post-processed with a specific Matlab code able to produce particular graphs to understand if the calibration has been performed successfully and to calculate the aimed calibration matrix. Figure 4.10 and 4.11 show the shaft calibration outputs for one of the G1 models. In the first one, the obtained data points are compared with theoretical values generated by the script and in the second, the errors between those two curves are plotted. To guarantee an accurate calibration, their standard deviations must remain under 2%.

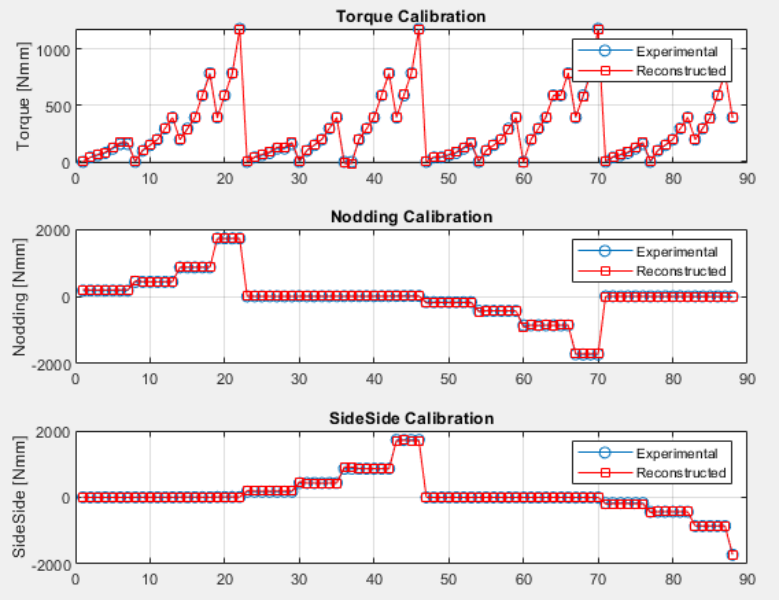


**Figure 4.10:** G1 M2 shaft calibration with reconstructed moments

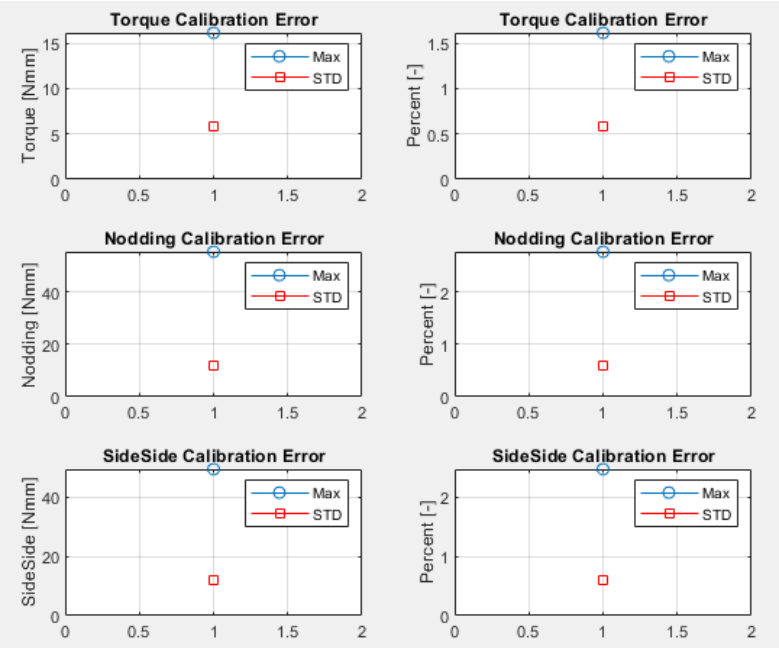


**Figure 4.11:** G1 M2 shaft calibration errors evaluation

### 4.2.5 Tower calibration

The aim and the concept behind the turbine tower calibrations are pretty similar compared to the shaft ones just described, or rather, to define the relationship between the voltage signals read by the strain gauges and the Wheatstone bridge and known loads, or moment forces, permitting for the assessment of the bending moments (FA and SS) acting on the turbine at the level of the tower basis.

To perform this operation, the turbine structure, connected to the Bachmann system, has been hung on the wall with the base facing it and the blades disassembled. For each of the four possible positions starting with the rotor facing up (0°, 90°, 180°, 270°), a magnetic hook has been used to apply a downward force, hanging then sequentially weights of different magnitudes (200g, 500g, 1kg, 1.5kg, 2kg) and the strain gauge signals have been recorded for each position. In addition to the weight, the other extremely relevant quantities to be measured for each turbine orientation have been the axial distance, or the position of the magnetic hook relative to the center of the strain gauges, which represents the "arm" length and the basis's inclination ($\theta$) relative to the horizontal direction. The latter has been measured using the usual digital inclinometer and is crucial to correct the turbine angular position and to have the actual correct orientation of the turbine hung. [46]

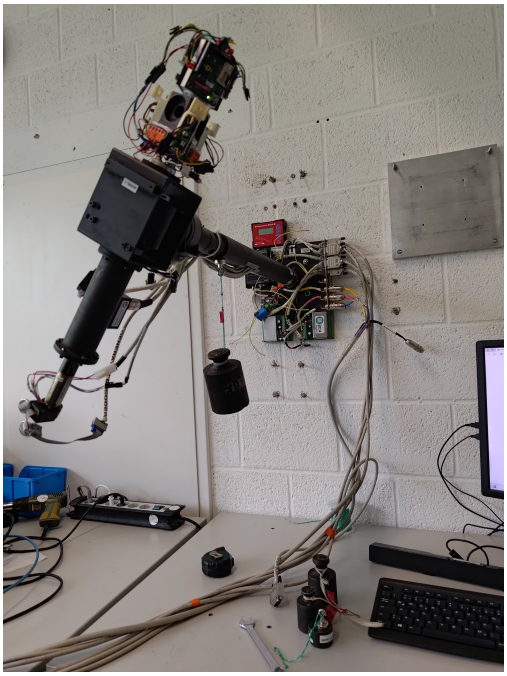

**Figure 4.12:** G1 tower calibration procedure

At each position, the offset has been first removed using the calibration software, and then the above measurements are recorded. These operations generate multiple measurement points, correlating the sensor responses in different directions to known weights and thus known forces.

The calibration matrix for the tower strain gauges results built in the following way:

$$\begin{pmatrix} M_{\text{Fore-Aft}} \\ M_{\text{Side-Side}} \end{pmatrix} = \mathbf{D}_{\text{matrix}} \cdot \begin{pmatrix} V_{\text{Fore-Aft}} \\ V_{\text{Side-Side}} \end{pmatrix} \tag{4.3}$$

From this, as both the applied moments and the measured voltages are known, the tower calibration matrix can be obtained as follows:

$$\mathbf{D}_{\text{matrix}} = \begin{pmatrix} V_{\text{Fore-Aft}} \\ V_{\text{Side-Side}} \end{pmatrix}^{-1} \cdot \begin{pmatrix} M_{\text{Fore-Aft}} \\ M_{\text{Side-Side}} \end{pmatrix} \tag{4.4}$$

Thanks to the calibration matrix, the control program is able to reconstruct the loads acting on the turbine tower basis during the working operations using the recorded voltages and subsequently calculate the errors incurred during the process. The collected data were then post-processed using Matlab to construct particular graphs (the obtained data points are compared with theoretical values generated by the script) to confirm the accuracy of the calibration and to calculate the aimed calibration matrix. The calibration is considered successful if the error standard deviations remain in a 1-2% range. Figure 4.13 and 4.14 show the shaft calibration outputs for one of the G1 models.

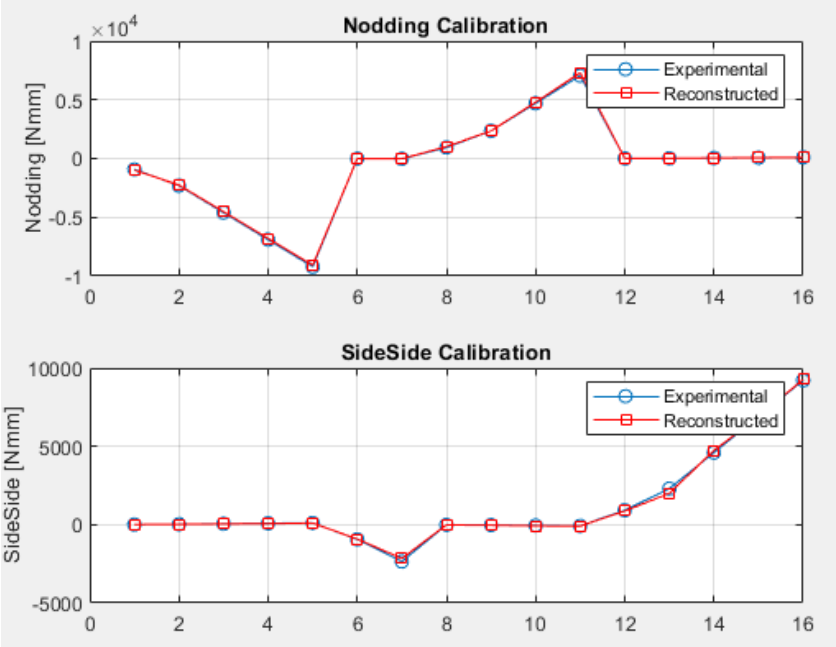


**Figure 4.13:** G1 M2 tower calibration with reconstructed moments

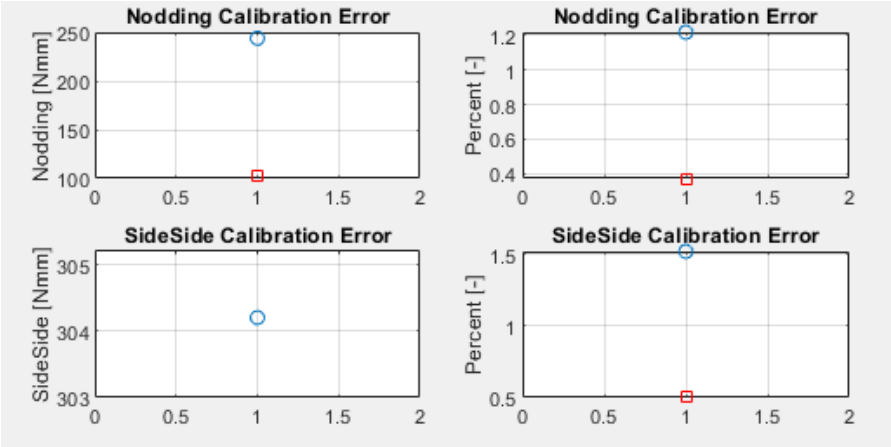


**Figure 4.14:** G1 M2 tower calibration errors evaluation

## 4.3 DIPC wind tunnel tests

The following sections will describe the wind tunnel campaign conducted in May and its results, concerning the exploration of the partially-bladed variation of the Helix technique and its combination with static derating to determine if these variants could lead to higher power gains.

### 4.3.1 Wind tunnel

The wind tunnel campaign conducted in May has been performed in the closed loop Wind Tunnel C of the Chair of Aerodynamics and Fluid Mechanics at TUM, whose characteristics are presented in Figure 4.16.

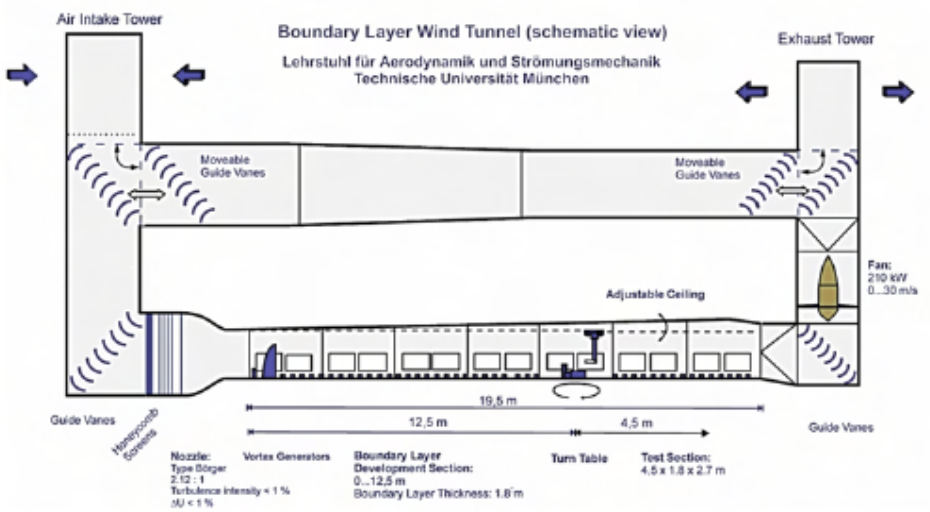


**Figure 4.15:** Schematic representation of Wind Tunnel 3 [47]

| Wind Tunnel Characteristics | |
|---|---|
| Cross-section of test section | 1.8m x 2.7m |
| Test section length | 21m |
| High turbulence intensity at hub height | ≈10% |
| Low turbulence intensity at hub height | <0.5% |

**Figure 4.16:** Wind Tunnel 3 characteristics [36]

In closed sections, such as a wind tunnel, the wind flow around the turbines can be influenced by the presence of walls. These walls constrain the flow to pass through a smaller area between the turbine and the walls, which tends to accelerate the wind and can affect the performance of the wind turbines during measurements. This phenomenon is known as the blockage effect and could be quantified by the so-called blockage ratio, $\alpha$, which is calculated as the ratio of the rotor area to the wind tunnel section:

$$\alpha = \frac{A_{\text{Rotor G1}}}{A_{\text{Tunnel}}} = 19.6\% \tag{4.5}$$

According to the literature, blockage effects can generally be ignored if the blockage ratio is below approximately 5% while for values close to $\alpha = 20\%$ it affects significantly the mean wind velocity and the wake expansion. [48]. To deal with this issue, a slightly lower rated wind speed with respect to the rated one for the G1 ($v_{rated} = 6\frac{m}{s}$) has been adopted to consider the acceleration due to the smaller section and also the Rotor Effective Wind Speed (REWS) for the upstream G1 turbine has been corrected, following the methodology outlined in Campagnolo et al. to guarantee a TSR close to the rated one during operations.[49]. It must be also specified that the whole campaign has been performed in conditions of low Ti.

### 4.3.2 Test setup and description

The two turbines have been positioned perfectly aligned in the central position of the channel and connected to the respective Bachmann cabinets and powered; the online interface has been then used to allow the manual and automatic control of the turbines during the tests. They were located at a distance of 5D since this results in the most suitable spacing in this wind tunnel for wake assessments and they were operated at the rated optimal conditions for this model to exploit their maximum potential in such tests. Basically, the upstream turbine has been operated by controlling it in accordance with the different Helix variants under investigation, while the downstream one has been used only as a power sensor. A Pitot tube was also adopted in the wind tunnel to achieve wind speed measurements during the tests. It was located at a distance of 4D before the turbine roughly at the same height as the rotor hub to avoid as many as possible wake disturbances but guaranteeing accurate measurements.

**Figure 4.17:** G06 shaft calibration

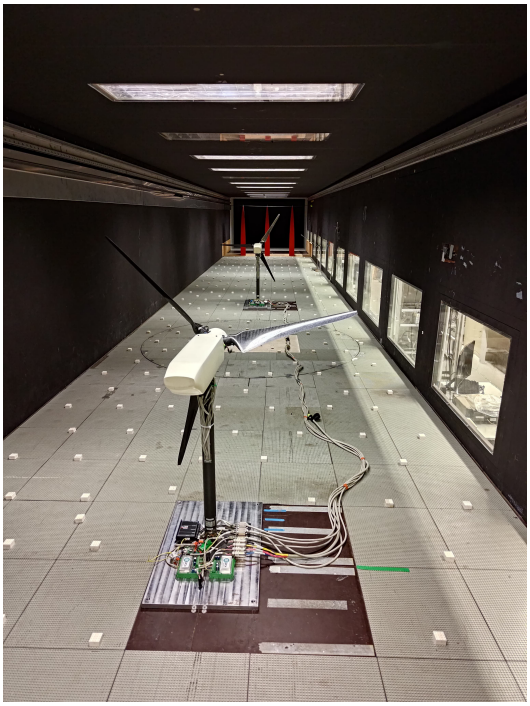

**Figure 4.18:** G06 tower calibration

The tests have been substantially two. During the first one, the DIPC technique was adopted firstly in the classic version and then dynamically modifying a lower number of blade pitch angles, experiencing a partially-bladed Helix. The idea after these is to ideally obtain a lower de-powering of the upstream turbine but still generate a helix wake. The second text instead, has explored still the Helix control technique, but letting the blades oscillate dynamically around a not-optimal pitch angle, in order to implement a sort of derating in the control technique. This would aim theoretically to a further de-powering of the upstream turbine to obtain a more substantial power gain in the downstream one.

### 4.3.3 Results discussion

The outputs of the tests regarding the comparison of the Helix technique involving a different number of blades are shown in Figure 4.19.

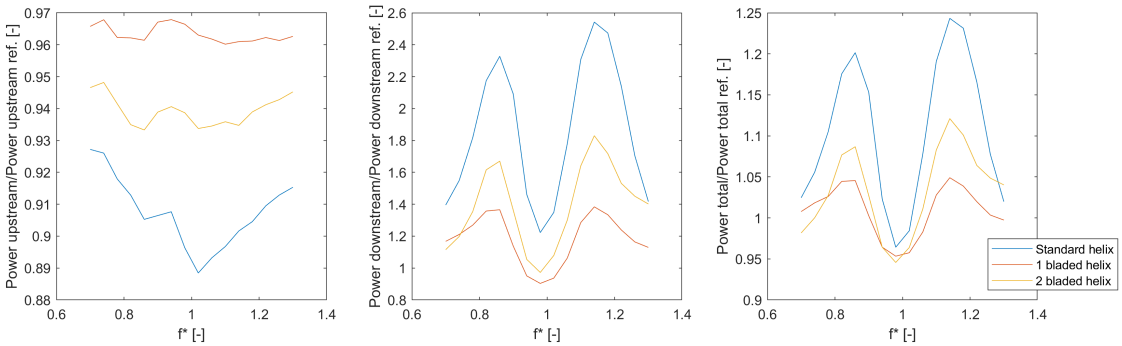


**Figure 4.19:** Normalized power outcomes using different Helix variants

How it is evident from the graph above, involving a smaller number of blades in the Helix control leads to a power gain of almost 10% (red line with respect to the blue one) for what concerns the upstream turbine, counterbalanced however by a power loss even ten times bigger than the gain for the downstream turbine. This behaviour also becomes more noticeable as the number of blades involved decreases. Indeed, as shown by the graph on the right in Figure 4.19, the overall normalized powers of the 1 and 2-bladed Helix result significantly lower with respect to the ones obtained with the classic approach that involves all three blades. It can be noticed how these results match ones experienced by Mühle et al. [33] regarding the actuation frequencies and the power gain peaks described before. Indeed, also these curves present power extraction peaks at sinusoidal excitation frequencies ($f_\beta$) of 0.88 and 1.12, which defines the CW and CCW Helix.
These tests result therefore relevant to understanding how the partially-bladed Helix doesn't show any particular gain and even brings to losses of power, confirming that the full-bladed Helix appears as one the most promising dynamic control techniques under investigation in these years. The unique benefit of involving only 1 or 2 blades in DIPC technique, could be represented by the lower wear and tear of the unused blade that can lead to a longer life of the components engaged and therefore, to a lower amount of maintenance or substitution of pieces needed.

Moving on to the second campaign of tests, the results concerning the integration of the full-bladed Helix with the induction technique are presented in Figure 4.20.

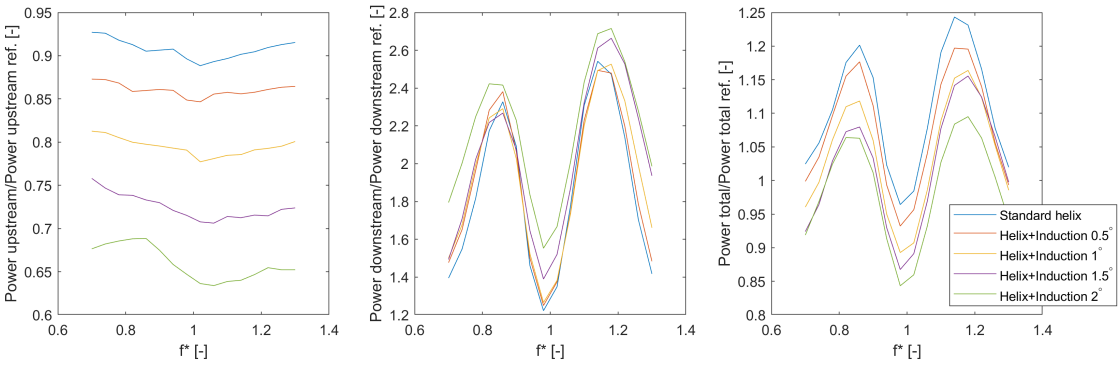


**Figure 4.20:** Normalized power outcomes combining Helix and induction control

In contrast to the trend described for the previous test campaign, letting the blades oscillate around at a not-optimal pitch angle, or basically increasing the induction or derating it, leads to power losses up to 50% with 2° of induction with respect to the standard Helix in the upstream turbine. The downstream turbine displays indeed power gains that reach however only values around 10%, and this happens only for the highest pitch angle differences, while inductions up to 1° don't exhibit any relevant power benefit.
Once again giving a glance at the graph on the right in Figure 4.20, it is evident how the standard Helix presents globally higher peaks in terms of achievable power, with gains in the order of 20-25% with respect to the implementation cases of high induction (blue line compared to the green one). Even though the induction technique has been shown relevant benefits on its own, combining it with the Helix, does not appear to yield any benefit and even it seems to reduce its effect. The reasons might be found in the fact that the induction technique would be aimed at decreasing the wind energy extracted by the upstream turbine, allowing it to operate in not-optimal conditions or optimal pitch, to have a lower impacting wake that could be converted into a higher amount of wind energy exploited by the downstream machine. However, the gains of the latter are significantly smaller compared to the loss of performance by the actuated turbine when this technique is combined with the Helix probably because the derating seems to hinder the wake helical manipulation, leading to the conclusion that this technique's integration doesn't seem worth the effort. Nothing excludes that these controls combined in a real scenario, where the wake mixing results higher due to more complex airflow interactions in the atmosphere, could reveal some benefit; but only further test campaigns in larger wind tunnel and with higher Ti could explore it.

# Chapter 5

# G06 TURBINE MODEL

## 5.1 Technical description and characteristics

The G06 wind turbine model represents a sophisticated, scaled-down turbine replica designed to produce realistic wakes, provide accurate load measurements and facilitate advanced testing scenarios in wind tunnel environments. Also this model has been completely designed and assembled in the Chair through the previous years and probably embodies the principal topic of this thesis.

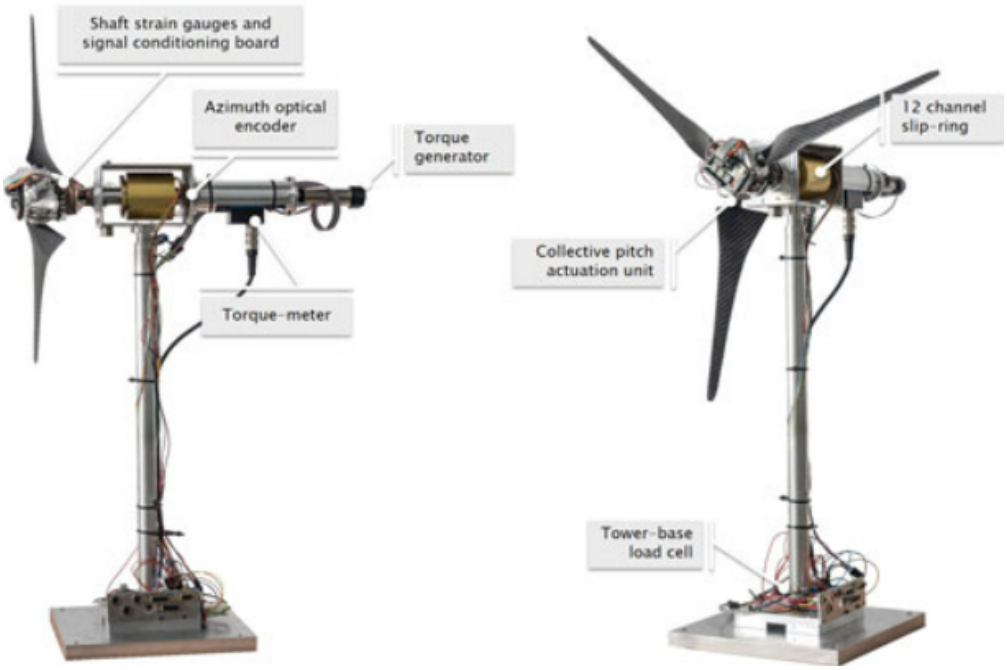


**Figure 5.1:** G06 wind turbine model [8]

It is also itself a scaled version of the DTU 10 MW wind turbine [9] and features an upwind three-bladed rotor with a diameter of 0.6 meters rotating clockwise and mounted on a tower that measures a height of 0.64 meters. Due to its small dimensions, the yaw actuator system has been located at the base of the model on a proper "yaw actuating basis" since an excessively out-of-scale tower could create a wider wake and has a mismatched vortex shedding. [50] The compact size and the adoption of a specific yaw actuating basis allowed the implementation of a more powerful motor and therefore it makes this turbine model extremely suitable for the investigation of new yaw-based control techniques as the dynamic yaw control. Figure5.2 illustrates the principal characteristics of this model. [8]

| G06 Turbine Characteristics | |
|---|---|
| Rotor diameter | 0.6 m |
| Hub height | 0.64 m |
| Rated power | 65 W |
| Rated wind speed | 10 m/s |
| Optimum TSR | 7.5 |

**Figure 5.2:** G06 main characteristics [8]

The G06 model is equipped with several advanced components and sensors of the same type and functioning as the ones previously described for the G1 model and the global architecture results therefore pretty similar, as for the rotor generator, the nacelle geometry, the torque meter, the azimuth optical encoder and the strain gauge locations and working principle. The main difference consists in the implementation of a collective pitch control mechanism, driven by a brushless motor located in the hub that adjusts all the 3 blades simultaneously by the same pitch angle through a gear system featuring a bevel driving gear that synchronizes the blades located on small driven bevel gears. Each blade was then outfitted with a Hall sensor to provide precise pitch angle measurements.
As for the G1, the shaft is equipped with three strain gauge sensors that measure the torque and the two bending moments previously discussed. These strain gauge signals are amplified by conditioning boards located inside the hub. The tower itself is also provided with strain gauges to detect the structural loads and they are situated in the basis interface, with their own conditioning boards.
Additionally, the G06 turbine shares with the G1 models also all the communication and control systems since the turbine is connected to the same control cabinet housing all the needed Bachmann PLC modules, described in the preceding chapter. This system aims to mirror those found in full-scale wind turbines, making the G06 a robust platform for simulating real-world turbine behaviour on a smaller wind tunnel scale. [8]

## 5.2 Technical improvements assembly procedure

During the months antecedent to this thesis, multiple technical improvements have been performed on the G06 model and so a new version of it has been then assembled, validated and tested as described in the following sections. The next paragraphs aim to briefly describe the optimizations made, followed by a complete and detailed walkthrough of the assembly and validation processes performed in these last months of work.

### 5.2.1 Improved and modified components

In previous wind tunnel tests, the pitch angle measurements provided by the Hall sensor at the root of each blade were unsatisfactory, with discrepancies between the requested and the measured angle increasing as the pitch angle and rotor speed rose, likely due to high centrifugal forces. To overcome this problem, it has been decided to substitute the Hall sensors system with an optical encoder at the root of each blade, being them able to guarantee incredibly higher accuracy, reliability and consistency in the measurements. It, being an optical monitoring device, required a larger housing space but didn't present issues regarding a possible not sufficiently satisfying linearity between the magnetic flux and the angular displacement as for the Hall sensor. [45] Accommodating the new devices has been therefore required multiple meticulous adjustments and a series of redesigns of the surrounding components, such as the hub itself. The implementation of optical encoders has forced the creation of more housing space and for this reason, the pitch shaft and bearing diameters have been reduced to fit these new components. These technical optimizations ensured that the distance between the hub and the blade tip remained unchanged to preserve the overall geometry and properties of the G06 model, as shown in Figure 5.3, 5.4 and 5.5.

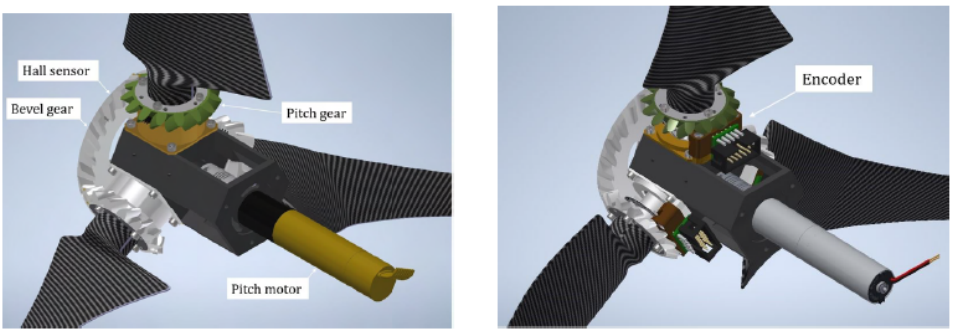


(a) Old configuration (b) New configuration

**Figure 5.3:** G06 hub modifications [28]

(a) Old configuration (b) New configuration

**Figure 5.4:** Hall sensor vs optical encoder [28]

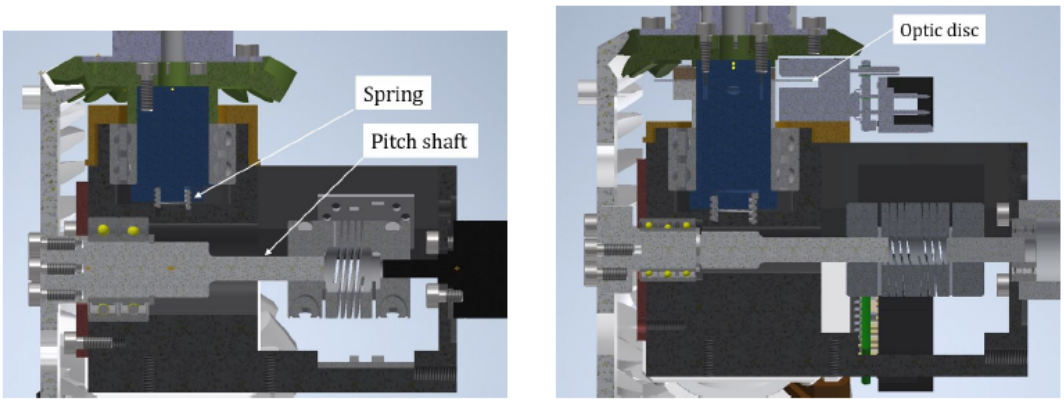


(a) Old configuration (b) New configuration

**Figure 5.5:** G06 hub sections [28]

The slip ring was the other component that caused the main issues. The previous version produced many signal transmission errors and its high friction due to the brush mechanism imposed the use of a proper cooling hydraulic system to avoid unpleasant overheating during the operations. Moreover, the high resistive torque caused a loss of power that diminished the amount of energy extracted by the rotor, making the turbines less efficient. To overcome these issues, a new slip ring model has been adopted by the department that guarantees reduced friction and a longer component lifespan due to the lower wear. [51] This new version results smaller in both outer and inner diameter, as well as in length and therefore, both the nacelle hollow case has been redesigned to house it and the pitch motor (from a brushless motor to a smaller but powerful brushed one) and the rotor shaft has been changed due to the limited space. Furthermore, a new smaller ball bearing, a smaller grooved nut and a redesigned distance ring have been selected to fit the new slimmer rotor shaft and to maintain the existing nacelle design. [28]

The following Figure 5.6 and 5.7 illustrate the technical improvements just described to allow a more concrete understanding.

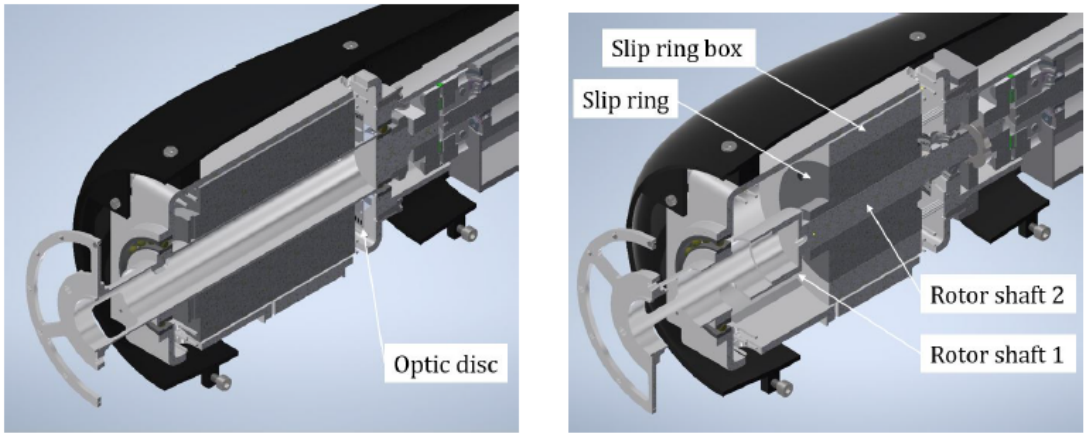


(a) Old configuration (b) New configuration

**Figure 5.6:** Slip ring and nacelle improvements [28]

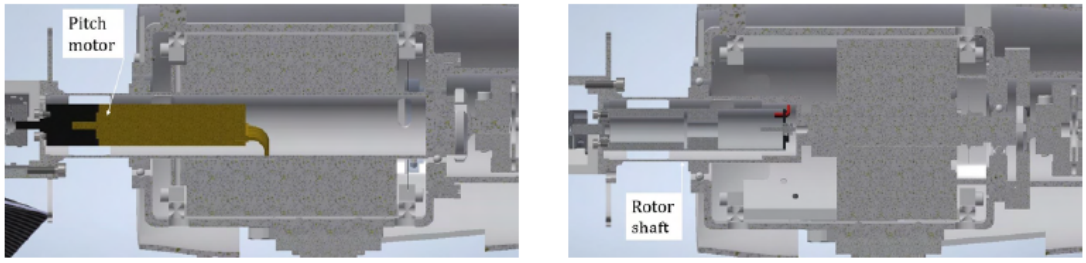


(a) Old configuration (b) New configuration

**Figure 5.7:** Section with new pitch motor [28]

### 5.2.2 Hub assembly

The first step was the hub assembly. The new pitch blade shafts, equipped with relative ball bearings, counteracting springs and custom-modified encoder disks have been inserted in the proper housings in the hub structure, as shown in Figure 5.8 and 5.9.

**Figure 5.8:** G06 pitch shaft spring

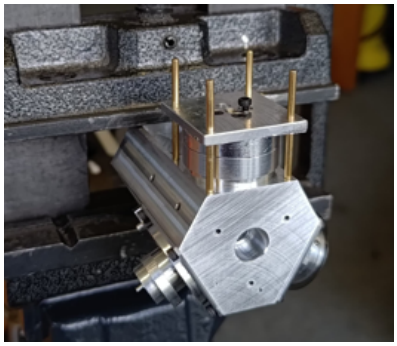

**Figure 5.9:** G06 pitch shaft insertion

The springs have the purpose of counteracting the force exerted by the pitch motor. During the last technical improvement, the existing ones were replaced with new ones provided with superior mechanical properties, such as enhanced maximum torque and elastic constant to eliminate any backlash in the system and guarantee a smoother actuation. Then the encoder chips were added together with the last portion of the rotor shaft, coupled with a small flexible joint to the new pitch motor. Arrived at this point, only the bevel gears were missing to complete the whole mechanical hub assembly and it was possible to work on the pitch controller and actuation part.

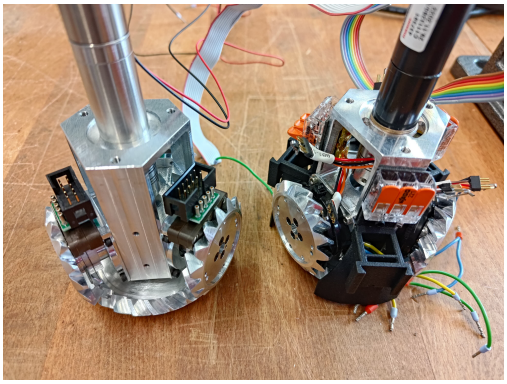

**Figure 5.10:** New (left) vs old (right) G06 hub assembly

### 5.2.3 Pitch controller gains tuning

Concluded the assembly of the hub, with the small bevel gears fastened on the 3 small shafts and the actuating big one on the end of the shaft connected to the pitch motor, it has been possible to verify the functioning of the encoder chips and tuning the controller gains. It must be also specified that to ensure a perfect coupling between the driving and driven gears, a small customized washer, used as a spacer, has been inserted under the big bevel gear to distance it more from the shaft while fastened.

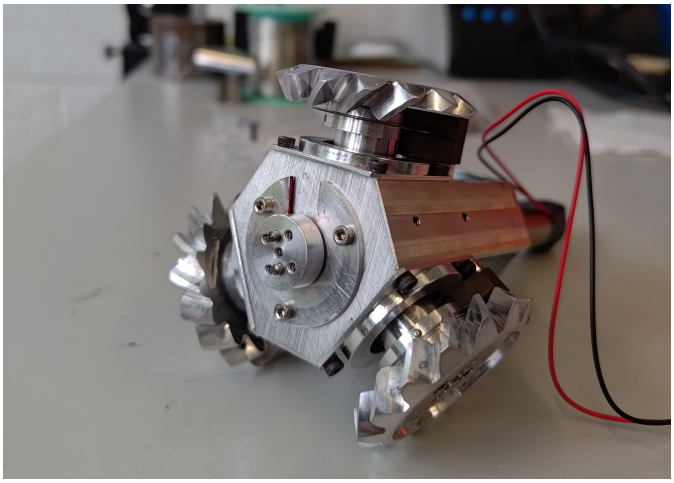

**Figure 5.11:** G06 hub with bevel gears

The hubs have been clamped with a vise to keep it stable and fixed during the activation of the pitch motor, as depicted in Figure 5.12. Then the control board has been connected to the motor, to one chip at a time, to the PC and powered with 24 V. Thanks to the board's proprietary Epos software, multiple homing procedures have been carried out to verify each chip's proper functioning and reliability. It is necessary that at least one per hub works since the pitch control is collective, but the larger the amount, the better the result.

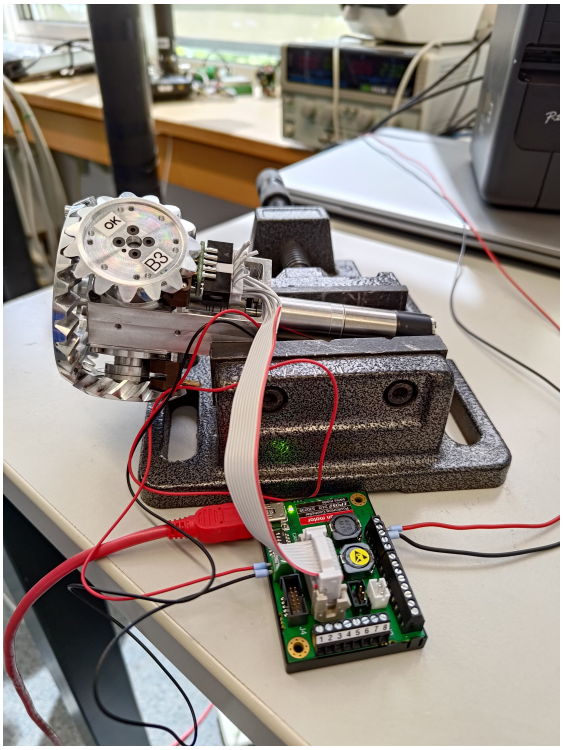

**Figure 5.12:** Pitch homing procedure for G06 hubs

The Homing procedure consists of allowing the pitch motor to spin till the encoder chip is able to detect the "0" notch on the disk, that position will be marked as the "home" one for what concerns the pitch and, starting from it, all the $\boldsymbol{\beta}$ angles will be identified.

The following step has been consisted of the actual tuning of the pitch controller gains. Being the controller a PID, it is provided by 3 different gains: [45]

- **Proportional gain ($K_p$):** expresses the magnitude of the response of the controller to the current error, adjusting the output proportionally to the error. The higher the $K_p$, the higher the system's responsiveness, but it can lead to overshooting and oscillations.
- **Integrative gain ($K_i$):** accumulates the past errors over time and integrates them to eliminate steady-state error, adjusting the output based on the cumulative error. A higher $K_i$ results in faster recovery of the steady-state error but can cause the system to become unstable if too high.

- **Derivative gain ($K_d$):** predicts the future trend of the error by considering its rate of change, and adjusting the output based on the rate of change of the error. A higher $K_d$ increases the system's damping capacity, reducing overshoot and oscillations, but it can also make the system sensitive to noise.

$$\text{Proportional Gain} \quad K_p: \quad u(t) = K_p \cdot e(t) \tag{5.1}$$

$$\text{Integral Gain} \quad K_i: \quad u(t) = K_i \cdot \int_0^t e(\tau)\, d\tau \tag{5.2}$$

$$\text{Derivative Gain} \quad K_d: \quad u(t) = K_d \cdot \frac{de(t)}{dt} \tag{5.3}$$

where u(t) represents the output function and e(t) the error one, defined as

$$e(t) = r(t) - y(t) \tag{5.4}$$

having r(t) as the input and y(t) as the output.

The combination of the all 3 gains in a PID controller is described by the following equation:

$$u(t) = K_p \cdot e(t) + K_i \cdot \int_0^t e(\tau)\, d\tau + K_d \cdot \frac{de(t)}{dt} \tag{5.5}$$

The board's proprietary Epos software allows the selection of 5 different setups for the 3 gains, basically tuning their "stiffness" or the responsiveness of the controller itself. The options start from the less aggressive response level (1) to the more aggressive one (5). As described above, increasing the stiffness of the gains can lead to overshoot and instability of the output, something really unpleasant during normal operations. Therefore proper tuning and a careful selection of the gains values are very relevant.

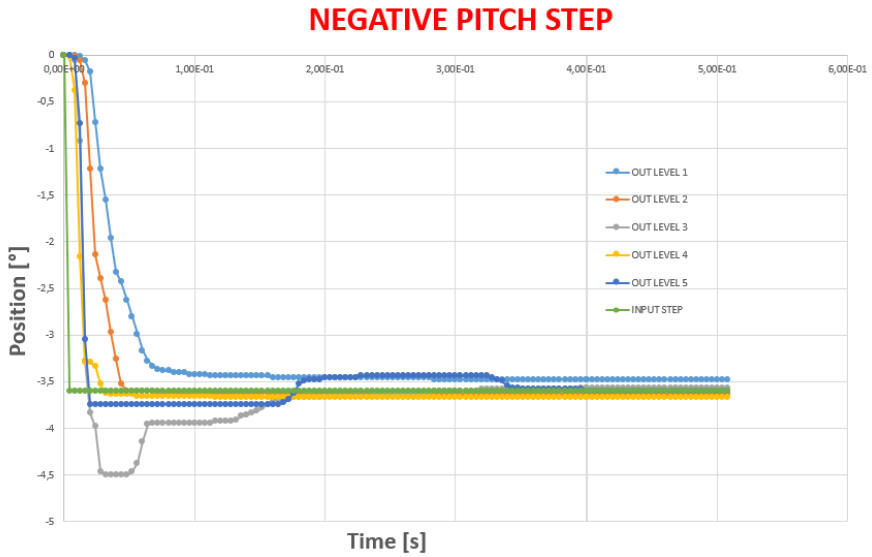


**Figure 5.13:** Pitch responses for a negative step request

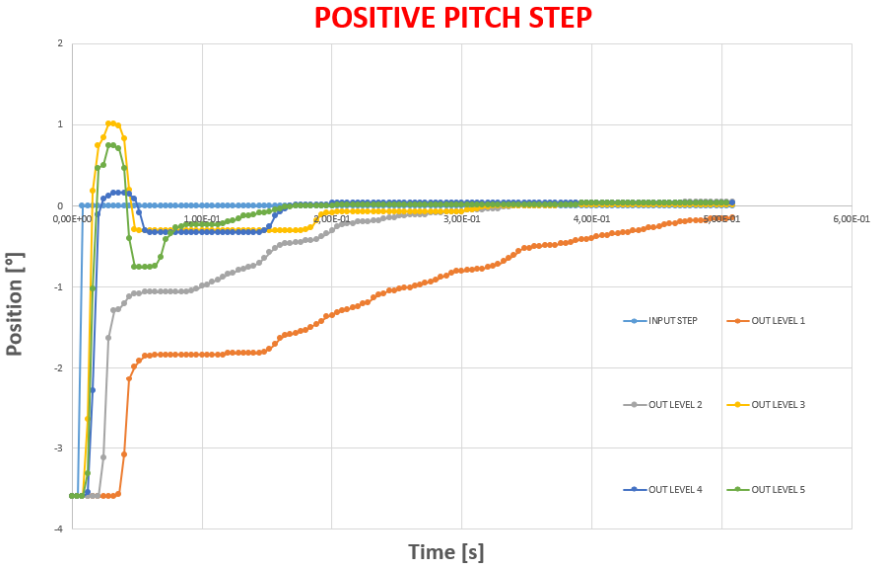


**Figure 5.14:** Pitch responses for a positive step request

As illustrated by Figure 5.13 and 5.14, an input step of 3.5° has been required for the motor of a hub, both against (negative step, from the 0° position the required one) and in favour (positive step, from the 3.5° position to the home one) of the action of the springs, with all the gain levels. The output data have been collected by the optical encoders and time response graphs have been created in order to

analyse the different setups. Both levels 1 and 2 didn't reveal adequate readiness, while the numbers 3 and 5 displayed an excessive overshoot and the presence of a certain instability in the settling of the signal. Therefore, the most suitable choice has been identified in the Stiffness Level 4, displaying great responsiveness with a reasonably low overshoot magnitude and steady-state error.

| Negative Settling Times [s] | | |
|---|---|---|
| | ±0.2° | ±0.1° |
| LEVEL 1 | 8,40E-02 | - |
| LEVEL 2 | 4,40E-02 | 4,40E-02 |
| LEVEL 3 | 1,52E-01 | 1,64E-01 |
| LEVEL 4 | 2,80E-02 | 2,80E-02 |
| LEVEL 5 | 2,00E-02 | 3,40E-01 |

**Figure 5.15:** Settling Times for negative pitch step

| Positive Settling Times [s] | | |
|---|---|---|
| | ±0.2° | ±0.1° |
| LEVEL 1 | 4,68E-01 | - |
| LEVEL 2 | 2,20E-01 | 2,76E-01 |
| LEVEL 3 | 1,88E-01 | 1,96E-01 |
| LEVEL 4 | 1,56E-01 | 1,60E-01 |
| LEVEL 5 | 1,20E-01 | 1,44E-01 |

**Figure 5.16:** Settling Times for positive pitch step

The two tables above present the different Settling Times achieved by the different gains levels. It refers to the time required for the output of a system to stabilize or settle within a certain percentage of its final value after a disturbance or a change in input. the tolerance bands are usually set within 2% or 5%, in our case it has been decided to consider an angle difference of $\pm 0.2°$ and $\pm 0.1°$ as plausible intervals. The Settling Time represents a great indicator of what concerns the system's readiness, and for this reason, it has been used in the evaluation just described. [45]

As stated before, Level 4 presents good results in terms of responsiveness, reaching average good times. The whole procedure has been carried out using a unique control board and then the correct parameters have been exported to the other boards.

### 5.2.4 Slip ring assembly and wiring

The following step consisted of the assembly and wiring of the slip rings, concluding the front and central parts of the nacelles. As previously described, the new slip ring has been assembled in the hollow case with the new inner rotor shaft on which the strain gauges are located and all this has been linked to a separating hollow disk and to the assembled hub. The purpose of such a disk is the possibility to use it for better cable layout and to add specific weights in particular radial positions to guarantee the rotor balancing, as explained in the next sections. The strain

gauge produces small voltage signals when the resistance bridge inside them is modified by mechanical strains, in our case small deformations generated by the loads on the rotor shaft. [45] These signals must be then amplified by specific conditioning boards, illustrated in Figure 5.17, able to amplify them due to their very low magnitude nature and sent to the control boards at the tower basis to be elaborated and show the actual present loads. To achieve this, these signals must travel inside the slip ring to reach the static part of the nacelle. Therefore, a special wiring layout has been arranged from scratch in order to connect the strain gauges to their conditioning boards and these latter components to the slip ring through special four-pin connectors.

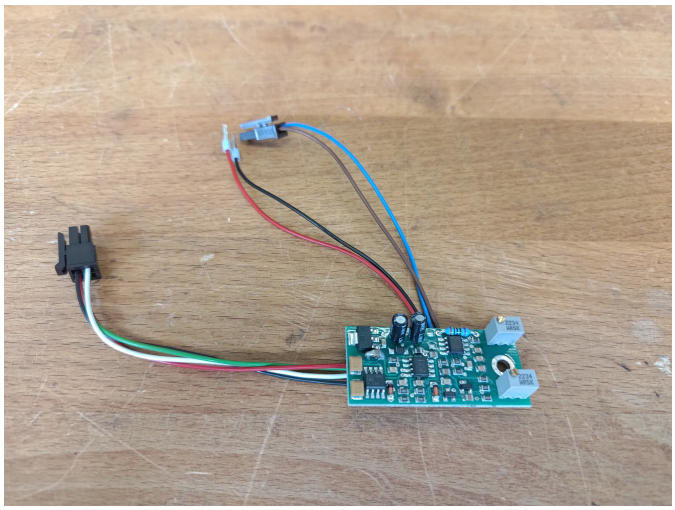

**Figure 5.17:** Strain gauge rotor conditioning board

The wiring creation and arrangement were a tricky and meticulous task for the contained dimensions and relevance of the components. It has been necessary to take into account the behaviour of the realized wires during rotation, making them as short as possible to avoid their dispersion and stretch due to the centrifugal force that can cause unpleasant disconnections. Lastly, the conditioning boards have been fixed and located in the inner part of the hub to protect them. The results of these operations are illustrated in Figure 5.18.

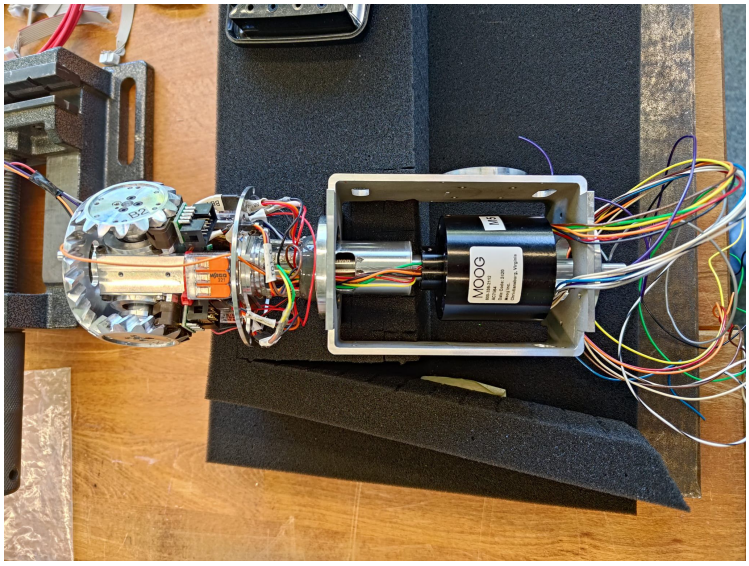


**Figure 5.18:** G06 slip ring wiring

### 5.2.5 Final parts assembly

Once reached this point, the remaining parts of the nacelle have been added, as the metal lateral cage that covers the slip ring and the cooling system plates applied on it. The cooling system is a hydraulic one, consisting of a pump that feeds a circuit with a special fluid with high thermal conductivity to dissipate the heat produced by the slip ring friction. Lastly, the nacelle has been completed with the rear block consisting of a hollow metal tube containing the rotor shaft extension, the torque meter and the rotor generator. The various parts of the axis result linked through flexible mechanical joints that allow small deformations and misalignments during the fast spinning, coupled with a good torque transmission.

**Figure 5.19:** flexible mechanical joint

The hollow metal cover tube instead has been connected by fastened flanges to ensure a solid connection. The whole nacelle has been then mounted on the proper tower and all the necessary wiring and connectors have been realized to connect all the boards, sensors, encoders and motors with the specific boards located on the actuating basis.

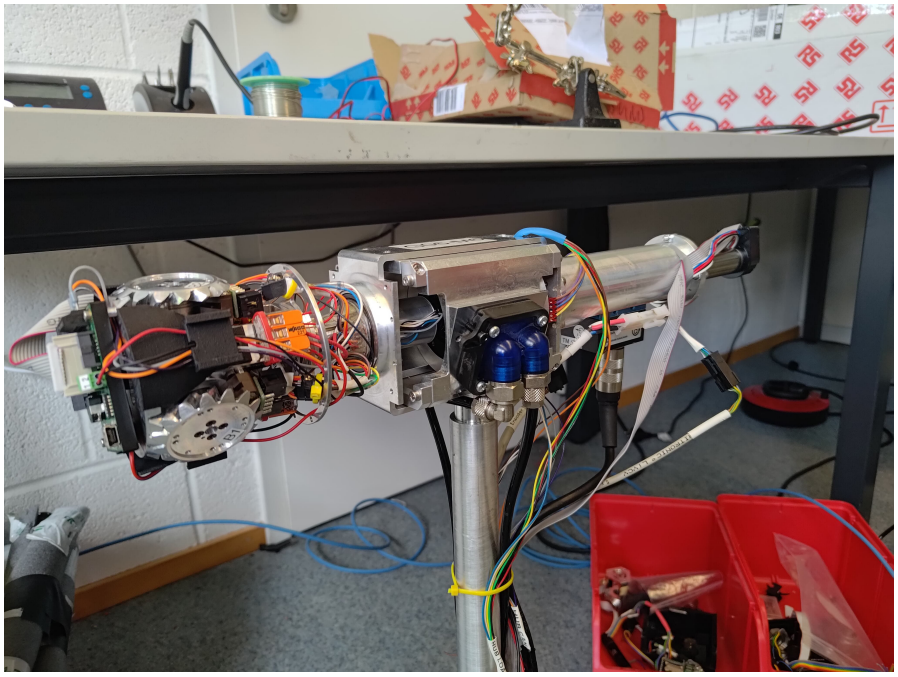

**Figure 5.20:** G06 nacelle and hub completed

Also the wirings present at the basis have been renovated and completely checked, especially the conditioning boards of the strain gauges at the tower basis have been substituted and welding operations were necessary.

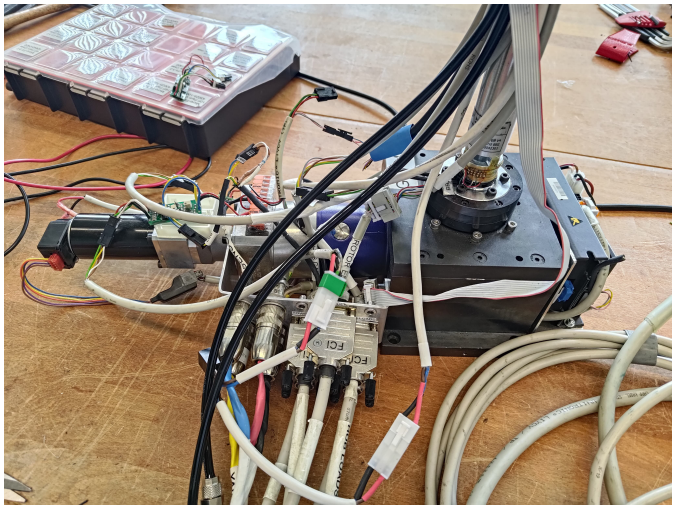

**Figure 5.21:** G06 yaw actuating basis

## 5.3 Sensor validation and calibrations

The 3 models are almost assembled and ready for the sensor inspection and calibrations.
Concerning the first operation, the models connected to the relative actuation bases and to the Bachmann have been turned on to perform a complete audit of all the sensors and encoders. The first that has been analyzed were the strain gauges present at the basis of the tower and on the rotor shaft. Applying small loads in different directions on the tower and on the hub, it was possible to access the correct functioning of the load sensors just mentioned, verifying if the FA and SS were correctly detected in the right orientations. Then, it was the turn of the rotor encoders to be checked. It has been ensured that the chips were able to read all the 20000 notches of the relative disks during the rotation, in order to allow the azimuth detection. Unfortunately, some disks have been damaged using the heat pistol during the slip ring wiring procedure and it has been necessary to disassemble partially the rear part of the nacelle to substitute them. Moreover, it has been noticed that the chips weren't always able to detect the "zero" notch (the one that allowed the reset of the azimuth count every complete rotation) during high-speed operations. The vibrations produced were such as to disturb the optical sensors of the chips and to slightly move it even if tightly fastened at the nacelle. To overcome this problem, it has been decided to modify somewhat the chips and add some glue in the threaded holes to dump small vibrations with respect to the whole structure. Lastly, also the yawing mechanism of the bases has been inspected for the correct functioning.

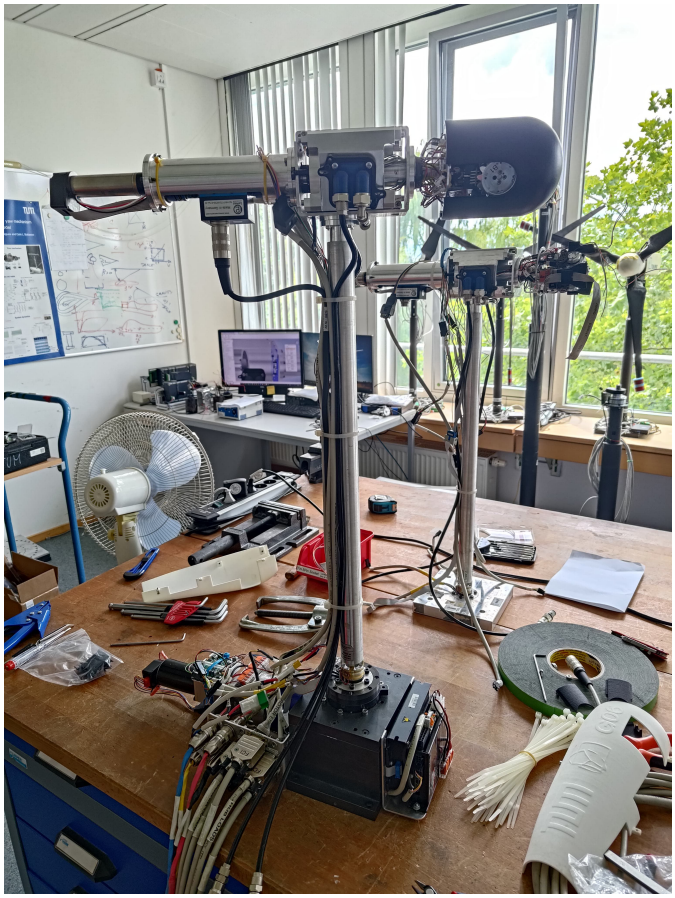

**Figure 5.22:** G06 almost assembled

The calibration operations were identical to the ones performed on the G1 models and presented in the previous chapter. Must be specified that the implementation of the optical encoder in place of the hall sensor for the pitch angle detection, has been made unnecessary the blade calibration since in optical sensors doesn't exist any correlation between electric signals and quantities measured, but only notches read from specific disks. The shaft and tower calibration for one of the models are illustrated in Figure 5.23 and 5.24.

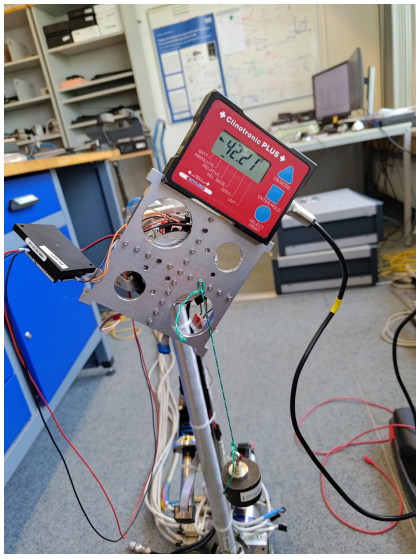


**Figure 5.23:** G06 shaft calibration

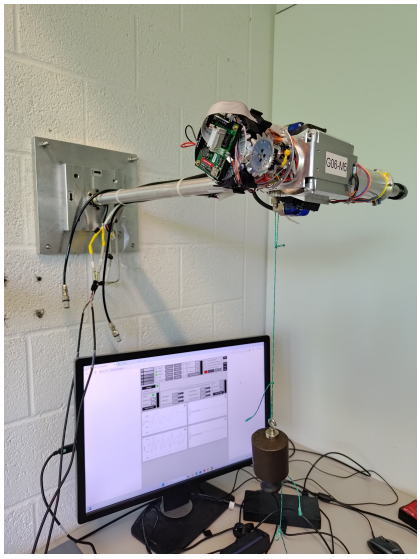

**Figure 5.24:** G06 tower calibration

## 5.4 New friction evaluation and blade angle setting

### 5.4.1 Friction test and comparison

The implementation of the new slip ring has been validated by doing dynamic sliding friction tests to confirm that the resistance torque during the rotation has been reduced with respect to the previous versions.
One at a time the turbines have been inserted into an acrylic glass box for safety reasons due to the very high rotational speed reached in the test, the aerodynamic hub cover has been applied and the holes due to the blade lack have been plugged using a tape in order to reduce as much as possible the air friction and avoid pumping effects during the operation. The turbines have been made to rotate from 200 rpm to 2200 rpm (close to the maximum velocity allowed by the machine) with steps of 200 rpm and the resisting torque, which identifies the dynamic sliding friction, has been recorded using the torque meter present in the nacelle.

**Figure 5.25:** G06 spinning for friction test

The resulting data has been post-processed through a specific Matlab code in order to obtain a plot showing the friction at different rotational speeds and compare it with the previous turbine version with the old slip ring mounted on, as shown in Figure 5.26.

The improvements are glaring with respect to the old models, with mechanical dynamic friction almost halved. It is also relevant to notice how the friction trend results essentially constant, increasing as the rotor speed increases, except for the presence of two peaks at around 800 and 1800 rpm. They represent the two rotor speeds that induce the resonance frequencies for respectively the tower and the rotor axis, especially where the rotor generator is located. These two conditions lead to high vibrations of the structure, causing stronger contacts and therefore higher friction recorded.

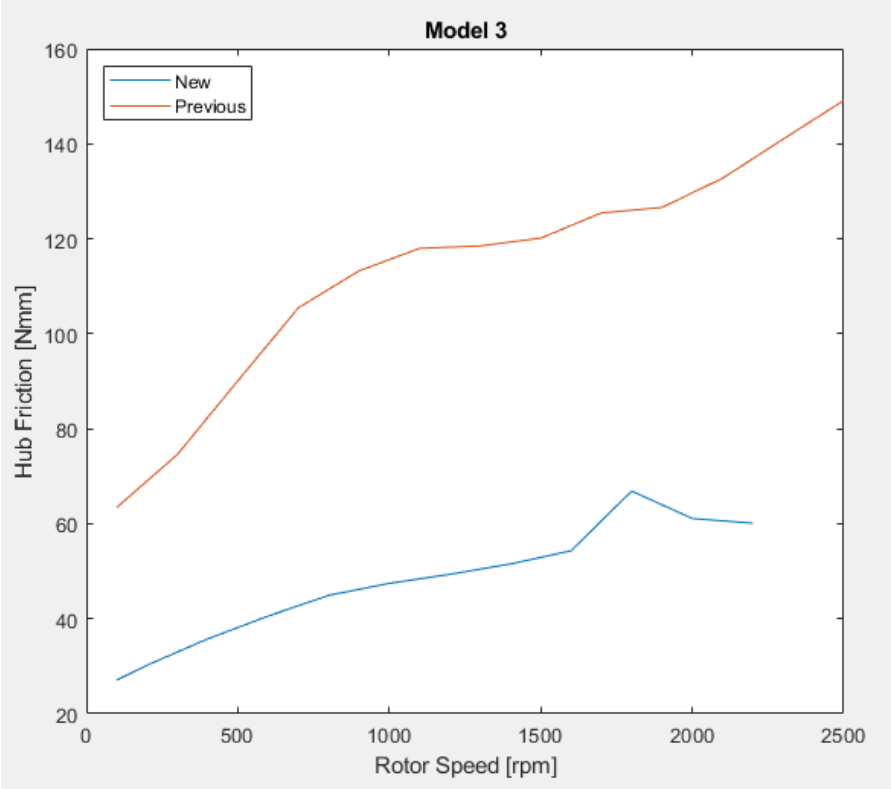


**Figure 5.26:** G06 friction comparison between old and new model

### 5.4.2 Blade angle of attack setting

The following step was the blade placement on the specific bevel gears on the hub. The blades are crafted from layers of pressed carbon fiber, and for this reason, it is very likely that their actual angle of incidence, or pitch angle, results differently. Dealing with a bladed rotor, even a small difference in AoI, or the angle between the blade's chord and the plane of rotation, among the blades can lead to high unbalance due to the different lift and thrust generated from each of them.[10] [41] Such unbalance, due to the high speed at which the rotor operates, would produce relevant tower moments that can affect the turbine operations and the sensors' functioning, as well as significantly higher stress on the structure and a reduction of the component's life. The blade root has been designed to be fastened on the bevel gears with four small screws, but the holes on the flange have been manufactured slightly larger than the ones actually required by such screws. This allows to have a small rotation freedom to scarcely adjust the AoI of each blade in order to reach a difference of at most $\pm 0.2°$, a satisfying result for such methodology.

| MEASUREMENTS WHILE ADJUSTING THE ANGLES | | | | | |
|---|---|---|---|---|---|
| | 1 | 2 | 3 | 4 | MEAN |
| BLADE 1 | 3.05 | 3.06 | 3.04 | 3.11 | 3.07 |
| BLADE 2 | 4.33 | 4.31 | 4.27 | 4.29 | 4.30 |
| BLADE 3 | 4.34 | 4.42 | 4.66 | 4.51 | 4.48 |
| | | | | TOT | 3.95 |

**Figure 5.27:** Example of pitch angle adjusting table

| MEASUREMENTS AFTER ADJUSTED THE ANGLES | | | | | |
|---|---|---|---|---|---|
| | 1 | 2 | 3 | 4 | MEAN |
| BLADE 1 | 2.81 | 2.77 | 2.83 | 2.84 | 2.81 |
| BLADE 2 | 2.91 | 2.93 | 2.90 | 2.86 | 2.90 |
| BLADE 3 | 2.92 | 2.91 | 2.93 | 2.89 | 2.91 |
| | | | | TOT | 2.88 |

**Figure 5.28:** Example of pitch angle adjusted table

Once hung the turbines on the wall with the hub pointing up to have the rotor in a horizontal position, one blade at a time has been installed and a homing procedure of the hub has been performed through the Epos pitch control board to bring the blade in the ideally "zero" pitch position. The actual pitch angle was then measured using a digital inclinometer positioned on a specific template that can be inserted around the blade. This operation aimed to detect the $\beta$-offset present for each blade by many measurements, in order to find a common mean one adjusting the blade fastening thanks to the small clearance present in the fastening holes. This value of $\beta$ has then been inserted into the pitch control code to remove the offset and to have precise adjustments of the pitch angle. The Figure 5.29 shows what just described.

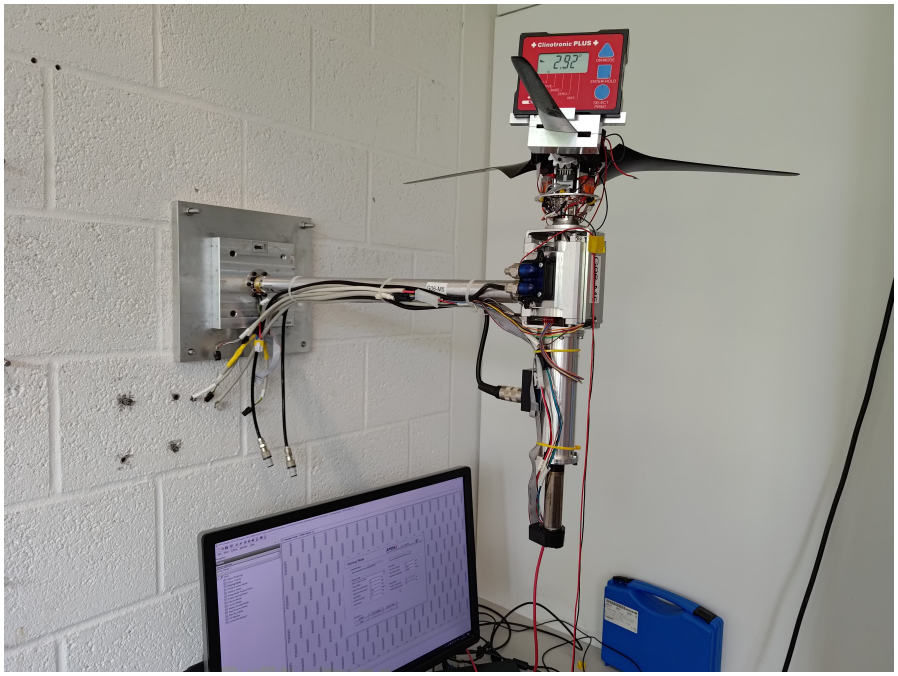


**Figure 5.29:** Blade pitch angle measurement

## 5.5 Rotor balancing

The presumable, even if small, weight difference among the blades and the asymmetrical position of the hub cables is enough to cause an unbalanced rotor with all the issues described in the previous subsection.

To avoid such an issue, the procedure has been the following. The turbine has been made to rotate at 700 rpm, which is an angular velocity that brings the tower close to its resonance frequency, to analyse the moments acting on the tower base when close to their highest values but without any risk of causing unwanted additional stress to the strain gauges.

Small weights modelled by a lead stripe and drilled, have been fastened to the crown behind the hub in variable azimuth configurations. The first step consisted of applying a 1 g weight in every azimuth position (from 0° to 330°, with a step of 30°) once per time, allowing the turbine to rotate into a very robust acrylic glass box for safety reasons and recording the loads. Through data post-processing using a specific Matlab code, the azimuth positions that lead to minimum moments have been detected, in order to define the operational interval (±30°).

**Figure 5.30:** Balancing weights positioning

The graph in Figure 5.31 presents angle-minimizing interval individuation for one of the models. On the ordinates are represented the tower moments FA and SS in [Nm], while on the abscissas the azimuth investigated angles in [°].

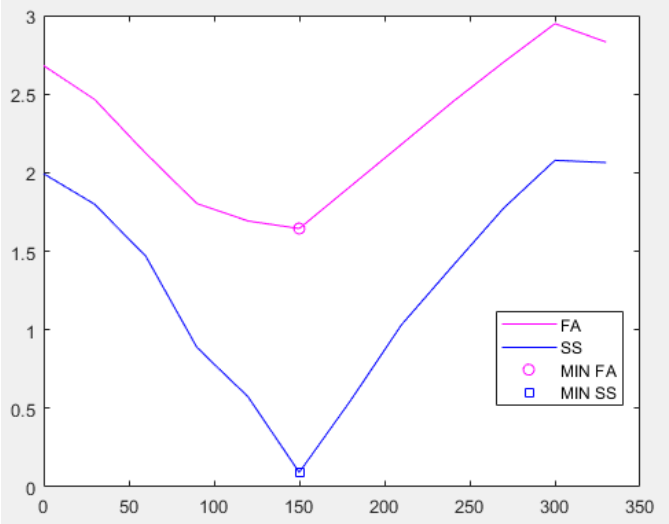


**Figure 5.31:** G06 M6 first balancing evaluation

Then, recordings with ever-increasing weights in the identified position intervals have been performed to observe the weights and position trends and their influence on the moments. Once the 2/3 best configurations have been detected, recordings with a speed of 800 rpm, or the speed that produces the tower resonance and therefore higher vibrations and loads at the basis, have been performed to obtain graphs concerning the balanced moments in the worst possible condition. It must be taken into account that the best configuration could turn out also in a divided weight between two adjacent positions since they are discrete, as actually happened for two models and shown in Figure 5.30. Moreover, it was preferred to minimize more the Side-Side moment with respect to the Fore-Aft. This is because the arm of the first is way longer than the one of the second, for the SS the arm is the whole tower height, while for the FA only the the distance between the rotor and joining point between the nacelle and the tower must be taken into account. Furthermore, the latter is more dumped in the normal operations by the aerodynamic interaction with the airflow.

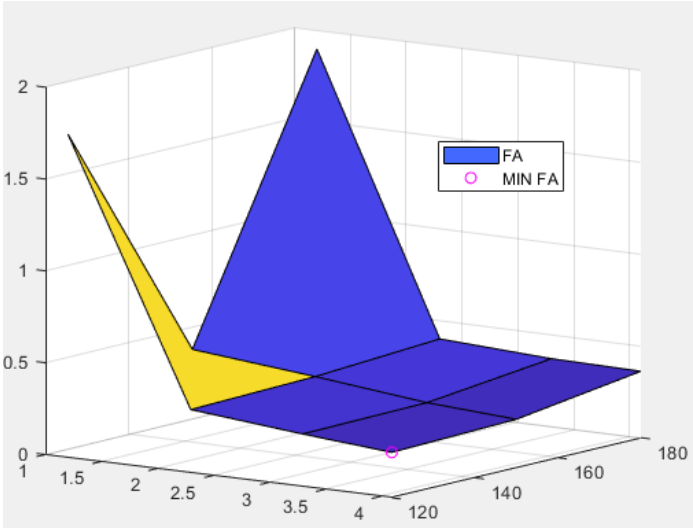


**Figure 5.32:** G06 M6 Fore-Aft trends evaluation

Figure 5.32 and 5.33 illustrate, through 3D graphs, the evaluation of the trend for the two tower bending moments, having the moments magnitude in [Nm] on the vertical axis and the angular azimuth position in [°] and the weights investigated in [g] on the two horizontal ones.

Lastly, the final tower moments evaluation is reported in Figure 5.34, with a graph similar to the one presented in Figure 5.31. It shows the best solution, as a compromise between the reduction of the two moments, for the balancing of this rotor which has resulted in a mass of 2 g at an azimuth of 150°.

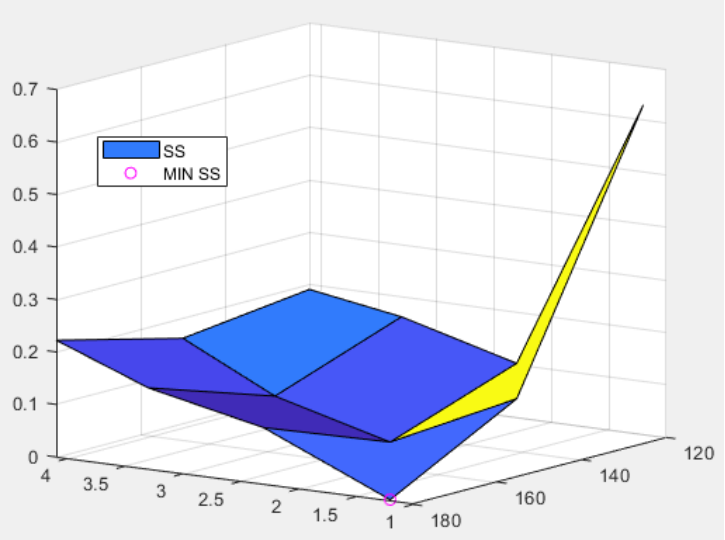


**Figure 5.33:** G06 M6 Side-Side trends evaluation

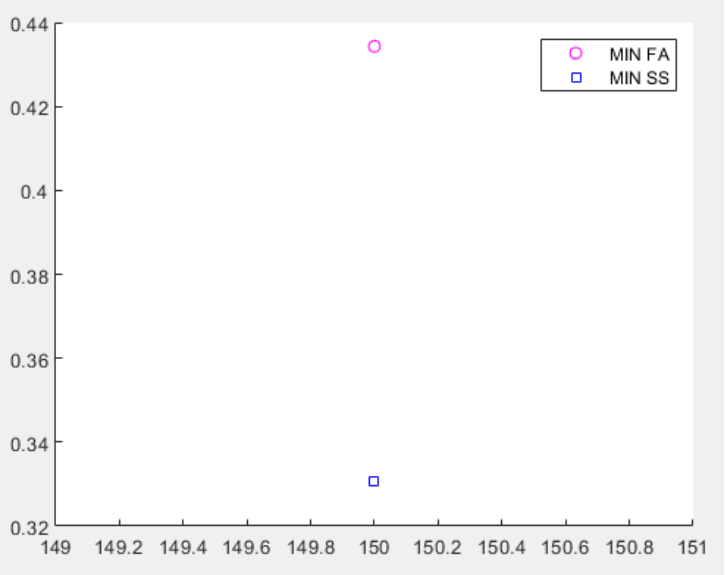


**Figure 5.34:** G06 M6 final tower moments evaluation at 800 rpm

This procedure basically recalls the balancing that is usually made to the car wheels, but with a more rudimentary approach since no complex software has been involved. This was the last operation done on the models, they resulted therefore completely assembled, checked, validated and ready for the operations in the wind tunnel.

## 5.6 Performance tests in the wind tunnel

The second wind tunnel campaign occurred in July and had the purpose of validating all the work done till here on the new model versions of G06 determining if the characteristics have been maintained also after the technical improvements and the new assembly procedure. To accomplish this, new performance and control strategy curves have been realized and compared with the ideal behaviour predicted by numerical simulations and with the previous models. It must be also specified that the experimental data could slightly deviate from the simulated ones due to differences in air characteristics (such as $\rho$ and T) of the test-specific day with respect to the ones adopted in the numerical evaluations.

### 5.6.1 Test setup

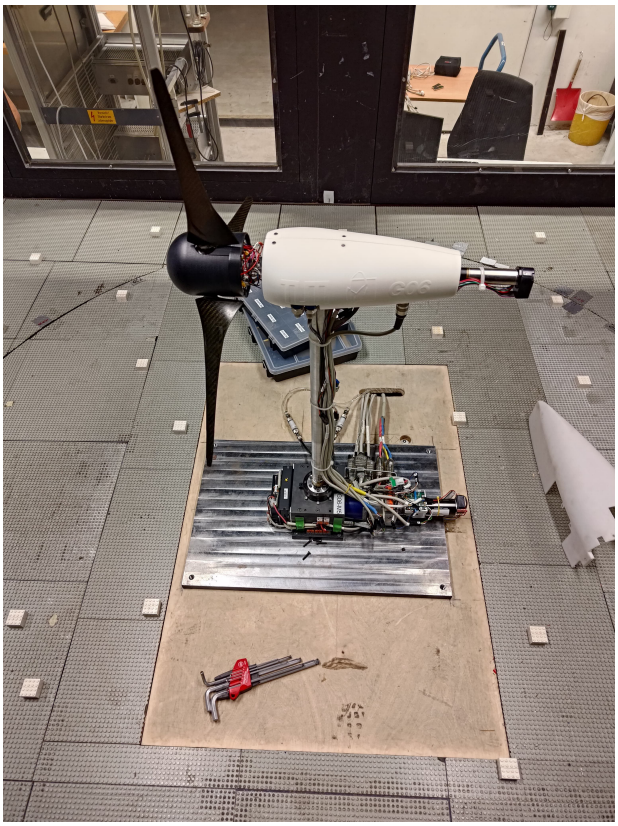

**Figure 5.35:** G06 completed during wind tunnel setup

The campaign was realized in the same wind tunnel used for the G1 (Wind Channel 3) and the experimental conditions were comparable to that previously described. It must be specified that since the blockage ratio in this setup was close to the negligibility threshold, the effects of blockage were considered null. The turbines, each per time, have been positioned in the middle point of the channel and perfectly oriented with the generated airflow. It was clearly connected to the Bachman cabinet and powered, the online interface was then used to allow the manual and automatic control of the turbines during the tests. A Pitot tube was also adopted in the wind tunnel to achieve wind speed measurements during the tests. It was located at a distance of 4D before the turbine roughly at the same height as the rotor hub to avoid as many as possible wake disturbances but guaranteeing accurate measurements. Moreover, the air conditions (as $\rho$ and T) have been measured and registered into the controlling software to be used for parameter calculations. Figure 5.35 and 5.36 show the turbine ready for the tests.

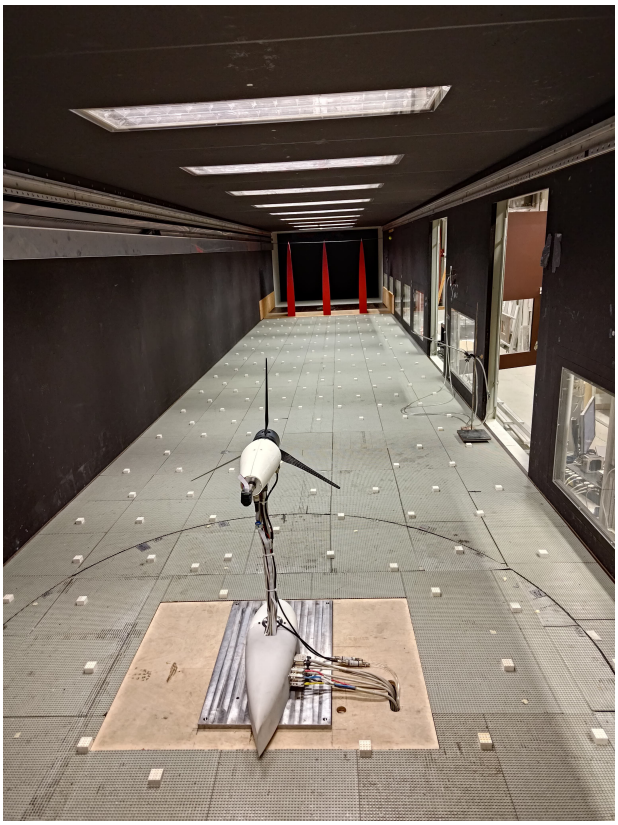

**Figure 5.36:** G06 in wind tunnel

### 5.6.2 Test description

The test aims to realize new performance and control strategy curves to evaluate all the relevant parameters during operations. Once completed the setup, the channel was turned on at low speed to warm up the models and avoid unwanted cranking stress. Different wind speeds have been investigated starting from 2.5 $\frac{m}{s}$ to the rated value of 10 $\frac{m}{s}$ with steps of approximatively 0.5 $\frac{m}{s}$. The rated power has been then overcome reaching 14 $\frac{m}{s}$ to perform the power derating and test also the new pitch actuation system based on optical encoders.

### 5.6.3 Results discussion

The curves obtained during the campaign are illustrated in the following figures, for easier comprehension the factors have been plotted directly versus the wind speed and error bars have been introduced to account for experimental uncertainties.

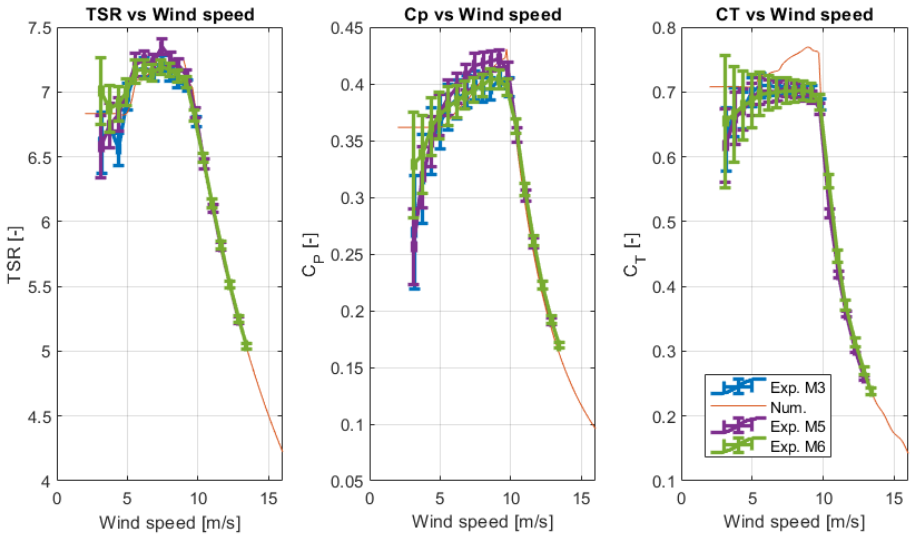


**Figure 5.37:** G06 new performance curves

The performance plots exhibit clearly that the new models perform perfectly and their characteristic performance parameters, the $C_P$, the $C_T$ and the TSR, replicate with high accuracy the numerical simulated values and result very close among the models, highlighting the precision and the accuracy of the assembly work performed on each of them. Indeed, the maximum TSR achieved is around 7.3, strictly similar to the design TSR* of 7.5, and the highest $C_P$ points result located in intervals around that value, confirming that the models´ performances reproduce those of the full-scale turbine in terms of efficiency and power extraction capacity. Moreover, peak $C_P$ values around 0.42 result in extremely high-performing for a scaled turbine and the correspondence between the model and the real turbine's performance at this rated TSR is evidence of the accuracy and effectiveness of the model's design. Also $C_T$ values exhibit a great consistency among the different models, not always predictable for hand-assembled machines equipped with custom-produced components. The unique relevant discrepancy with the numerical simulation occurs with the $C_T$ values obtained in the wind speed span between 5 and 10 $\frac{m}{s}$. The more reasonable explanation for this is an overestimate by the numerical models of lift generated by the blades in the Reynolds conditions corresponding with such a wind velocity span, with the lift as the major factor that influences the thrust.

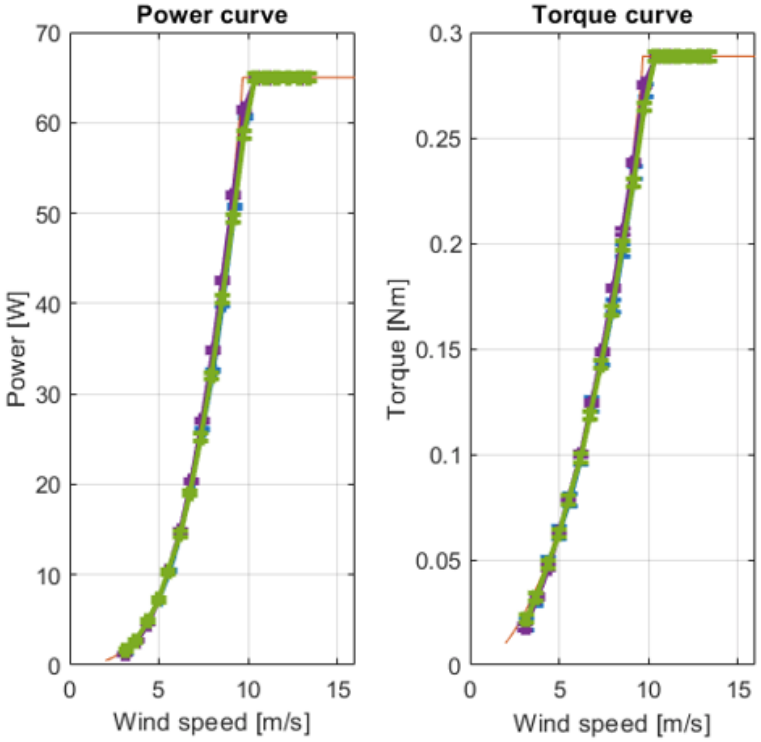


**Figure 5.38:** G06 new control strategy curves part 1

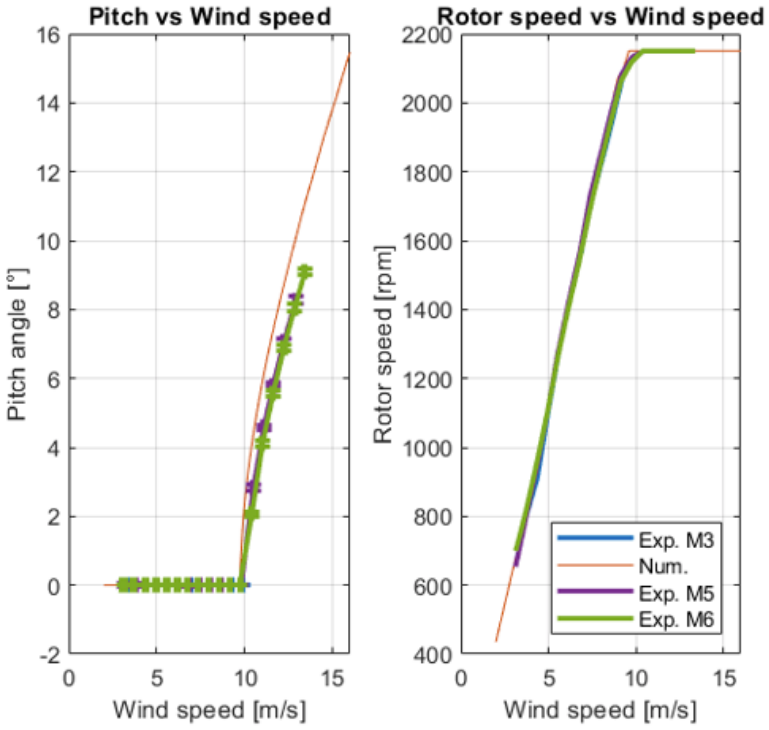


**Figure 5.39:** G06 new control strategy curves part 2

The control strategy curves depicted in Figure 5.38 and 5.39 show how well and consistently the 3 new models operate and perform, with all three curves practically superimposed among them. The power and torque curves behave almost perfectly as described and by the theoretical equations, with a rising initial trend that follows respectively the third and the second power of the wind velocity (Equation 2.6 and 2.9). Also the rotor speed exhibits this consistent attitude, increasing linearly till it reaches the rated value around 2100 rpm with a linear growth with respect to the wind speed as imposed by the constant TSR control strategy adopted in Region 2 of the control techniques, explained in the Chapter 2. It is effortless to notice how the pitch control steps into the control strategy when the rated power, torque and rotor speed are approached. There, the pitch motor starts twisting the blade in order to derate the energy extraction and maintain the power constant at its rated value of 68 W (Region 3) even if the wind speed exceeds the nominal one and could cause overloads in the components. The pitch curve illustrates how this occurs, with a prompt increase in the $\boldsymbol{\beta}$ angle after the 10 $\frac{m}{s}$ of wind speed is reached. The actual machine curves slightly deviate from the ideal one due to an overestimation of the pitch actuation response by the numerical model, nevertheless, the integration of new optical encoders and a new motor guarantees smoother control and higher promptness and readiness with respect to the old version with

hall sensors, achieving also a stronger consistency during the operations. The old architecture generated some fluctuation in the constant power region, while now the curves lay perfectly flat.

All these very satisfying results are the crowning of all the assembly, calibration and validation works done in the previous months combined with the design operations accomplished previously in the Chair. This establishes the robustness and reliability of the improved G06 models, capable of guaranteeing the rated characteristics with higher performances and consistency thanks to the technical improvements implemented. The models resulted therefore completely settled and ready for shipment to the Texas University in Dallas (USA) for further experiments due to the awesome research collaboration between the two institutions.

# Chapter 6

# CONCLUSIONS

This project had the purpose of providing a deep insight into the world of scaled wind turbines and their pivotal role in wind tunnel test scenarios. Every practical aspect has been investigated during this journey, giving an idea of what dealing with real machines means.

Firstly, the data post-processing of the characteristics of a new multi-hole probe for wind speed and direction detection depicted how modern sensors such that one are able to supply accurate and consistent experimental data on this type of scaled device data and the implementation for future operations can turn into a winning choice. All the assembly, wiring, tuning and validation work done on the two scaled turbine models; the G1 and the G06, highlighted the multidisciplinary nature of such devices and how complex and challenging it turns out to be the achievement of a versatile and realistic representation of a wind turbine with all the different components that characterize them. The calibration procedures revealed that such processes are not merely technical procedures but also crucial in ensuring the reliability and consistency of the data collected. Through these rigorous processes, trustworthy and accurate sensor data can be acquired, greatly contributing to the credibility of the experimental outcomes. Then, the practical assembly and integration of all the subsystems that make up this scaled model highlighted all the hands-on challenges, especially regarding the new technical improvements in the G06, that could arise during a machine realization, with the necessity of accurately merging the mechanical, electrical and control aspects. Moreover, all the inspections and tests validated the improvements and depicted how the implementations of a new pitch control mechanism and its tuning, the technical hub optimizations and the adoption of a new slip ring guarantee a superior and more consistent control twist capacity combined with better signal transmissions, reduced rotational friction, lower resisting torque and longer component lifespan. The culmination of this project consisted then of the two wind tunnel test campaigns

conducted in May and July. The first one explored new variants of the Helix theory through DIPC in a partially-bladed version or combined with derating. However, the tests unfortunately revealed that the Helix control technique performs at its best in its classic variant since the partial-bladed version has proven inadequate for a consistent helical meandering of the wake and the implementation of the derating seems to even hinder the technique targets. The second campaign had the purpose instead of accessing the performance and control strategy curves of the improved G06 models to confirm and validate their reliability and functioning. The curves came out absolutely fulfilling, demonstrating the robustness and reliability of the improved G06 models, capable of guaranteeing the rated characteristics with higher performances and consistency also after the technical improvements were implemented.

During this dissertation, many new challenges and prospects have been presented regarding the wind energy sector, particularly concerning the feasibility and in-depth understanding of advanced techniques for wind farm power optimization. Only further research, studies and tests will be able to explore them, with the hope that this work could contribute, even if only in its own small way, to future experimental achievements.

# Bibliography


[1] UNFCC. «Cut global emissions by 7.6% every year for next decade to meet the 1.5°C Paris target». In: (2019) (cit. on p. 1).

[2] European Commission - Renewable energy targets. *https://energy.ec.europa.eu/topics/renewable-energy/renewable-energy-directive-targets-and-rules/renewable-energy-targets-en* (cit. on p. 1).

[3] European Comission. «2030 climate  energy framework». In: (2020) (cit. on p. 1).

[4] Energy-Charts. $https://energy\text{-}charts.info/charts/energy_pie/chart.htm?l = enc = EUinterval = yearyear = 2023$ (cit. on p. 2).

[5] GWEC. «Global wind report 2022 by Global Wind Energy Council». In: (2022) (cit. on p. 3).

[6] M. F. Howland, S. K. Lele, and J. O. Dabiri. «Wind farm power optimization through wake steering». In: *Proceedings of the National Academy of Sciences of the United States of America* 116 (2019) (cit. on pp. 3, 17).

[7] R. J. Barthelmie et al. «Modelling and measuring flow and wind turbine wakes in large wind farms offshore». In: *Wind Energy* 12 (2009) (cit. on p. 3).

[8] E. Nanos, C. Bottasso, F. Campagnolo, S. Letizia, G. Iungo, and M. Rotea. «Design, steady performance and wake characterization of a scaled wind turbine with pitch, torque and yaw actuation». In: *WES* 7.3 (2022) (cit. on pp. 4, 6, 42, 46, 59, 60).

[9] C. Bak et al. «The DTU 10-MW reference wind turbine». In: *Danish Wind Power Research* (2013) (cit. on pp. 5, 39, 60).

[10] J.F. Manwell, J.G. McGowan, and A.L. Rogers. *Wind Energy Explained*. Amherst, USA: John Wiley & Sons Ltd, 2002 (cit. on pp. 5, 7–10, 31, 32, 77).

[11] C. L. Bottasso and F. Campagnolo. «Wind Tunnel Testing of Wind Turbines and Farms». In: *Handbook of Wind Energy Aerodynamics*. Ed. by B. Stoevesandt, G. Schepers, P. Fuglsang, and Y. Sun. Cham: Springer International Publishing, 2022 (cit. on p. 5).

[12] M. O. L. Hansen. *Aerodynamics of wind turbines*. London: Earthscan, 2008 (cit. on pp. 7, 8).

[13] A. Betz. «Schraubenpropeller mit geringstem energieverlust dissertation». PhD thesis. 1919 (cit. on p. 9).

[14] T. Burton, D. Sharpe, N. Jenkins, and E. Bossanyi. *Wind Energy Handbook*. Chichester, England: John Wiley & Sons Ltd, 2001 (cit. on pp. 10–13).

[15] J. Meyers, C. Bottasso, K. Dykes, P. Fleming, P. Gebraad, G. Giebel, T. Göçmen, and J.W. van Wingerden. «Wind farm flow control: prospects and challenges». In: *WES* 7.6 (2022) (cit. on pp. 14–17, 19–21, 24, 25).

[16] S. Kanev, E. Bot, and J. Giles. «Wind farm loads under wake redirection control». In: *Energies* 13.16 (2020) (cit. on pp. 14, 15).

[17] R. J. Barthelmie et al. «Modelling and measuring flow and wind turbine wakes in large wind farms offshore». In: *Wind Energy* 12.5 (2009) (cit. on p. 15).

[18] J. Annoni, P. M. O. Gebraad, A. K. Scholbrock, P. A. Fleming, and J. W. v. Wingerden. «Analysis of axial-induction-based wind plant control using an engineering and a high-order wind plant model». In: *Wind Energy* 19.6 (2016) (cit. on p. 17).

[19] Gebraad, J. J. Thomas, A. Ning, P. Fleming, and K. Dykes. «Maximization of the annual energy production of wind power plants by optimization of layout and yaw-based wake control». In: *Wind Energy* 20.1 (2017) (cit. on p. 17).

[20] F. Campagnolo, V. Petrovic, C. L. Bottasso, and A. Croce. «Wind tunnel testing of wake control strategies». In: *ACC 2016* (2016) (cit. on p. 17).

[21] Siemens Gamesa. *Siemens gamesa now able to actively dictate wind flow at offshore wind locations*. 2019 (cit. on p. 17).

[22] R. Nouri, A. Vasel-Be-Hagh, and C. L. Archer. «The Coriolis force and the direction of rotation of the blades significantly affect the wake of wind turbines». In: *Applied Energy* 277 (2020) (cit. on p. 18).

[23] E.M. Nanos, C. L. Bottasso, S. Tamaro, D. I.Manolas, and V. A. Riziotis. «Vertical wake deflection for floating wind turbines by differential ballast control». In: *Wind Energy Science* 7.4 (2022) (cit. on pp. 18, 19).

[24] G. Armengol Barcos and F. Porté-Agel. «Enhancing wind farm performance through axial induction and tilt control: Insights from wind tunnel experiments». In: *Energies* 17.1 (2024) (cit. on p. 19).

[25] V. Strouhal. «Ueber eine besondere art der tonerregung». In: *Annalen der Physik und Chemie* 241.10 (1878) (cit. on p. 19).

[26] J. A. Frederik, R. Weber, S. Cacciola, F. Campagnolo, A. Croce, C. Bottasso, and J.W. van Wingerden. «Periodic dynamic induction control of wind farms: proving the potential in simulations and wind tunnel experiments». In: *WES* 5.1 (2020) (cit. on pp. 19, 20).

[27] «An optimal control framework for dynamic induction control of wind farms and their interaction with the atmospheric boundary layer». In: *Philosophical Transactions of the Royal Society A: Mathematical, Physical and Engineering Sciences* 375.2091 (2017) (cit. on p. 20).

[28] Martin Pasko. «Experimental wind tunnel study on the combination of static and dynamic wake control techniques for wind turbines». TUM, 2024 (cit. on pp. 20, 22, 24, 25, 61–63).

[29] Munters and Meyers. «Dynamic strategies for yaw and induction control of wind farms based on large-eddy simulation and optimization». In: *Energies* 11.1 (2018) (cit. on pp. 21, 25).

[30] A. Croce, S. Cacciola, M.Montero Montenegro, S. Stipa, and R. Praticó. «A CFD–based analysis of dynamic induction techniques for wind farm control applications». In: *Wind Energy* (2022) (cit. on p. 21).

[31] J. A. Frederik, B. M. Doekemeijer, S. P. Mulders, and J. W. Wingerden. «The helix approach: Using dynamic individual pitch control to enhance wake mixing in wind farms». In: *Wind Energy* 23.8 (2020) (cit. on pp. 21, 23).

[32] H. Korb, H. Asmuth, and S. Ivanell. «The characteristics of helically deflected wind turbine wakes». In: *Journal of Fluid Mechanics* 965 (2023) (cit. on pp. 21, 23).

[33] F. V. Mühle, F.M.Heckmeier, F. Campagnolo, and C. Breitsamter. «Wind tunnel investigations of an individual pitch control strategy for wind farm power optimization». In: *WES* 9.5 (2023) (cit. on pp. 21–24, 40, 56).

[34] D. van der Hoek, B. V. den Abbeele, C. Simao Ferreira, and J. W. van Wingerden. «Maximizing wind farm power output with the helix approach: Experimental validation and wake analysis using tomographic particle image velocimetry». In: *Wind Energy* 27.5 (2024) (cit. on p. 23).

[35] M. F. Howland, A. S. Ghate, S. K. Lele, and J. O. Dabiri. «Optimal closed-loop wake steering – part 1: Conventionally neutral atmospheric boundary layer conditions». In: *WES* 5.4 (2020) (cit. on p. 24).

[36] Flavia Klinger. «Experimental wind tunnel study of the dynamic yaw control technique, for faster wake recovery». TUM, 2023 (cit. on pp. 25, 53).

[37] Vectoflow GmbH. *Probe Manual - Version 2021-10-27* (cit. on pp. 27, 28).

[38] I. Care and F. Fourneaux. «Investigation of the pressure response of different Pitot tubes». In: *Flow Measurement and Instrumentation* 72 (2020) (cit. on pp. 29–31).

[39] MOOG - Slip rings with through-bores. *https://www.moog.com/content/dam/moog/literature/MCG/DtS_AC6438.pdf* (cit. on p. 30).

[40] eFunda - engineering fundamentals. *https://www.efunda.com/designstandards/sensors/pitot.tubes/pitot.tubes.theory.cfm* (cit. on p. 30).

[41] Gary L. Johnson. *Wind Energy Systems*. Manhattan, KS: Electronic Edition, 2006 (cit. on pp. 31, 77).

[42] https://www.nrgsystems.com/products/met-sensors/detail/nrg-200m-wind-direction-vane. *NGR Systems* (cit. on p. 31).

[43] F. Campagnolo, V. Petrovic, J. Schreiber, E. M. Nanos, A. Croce, and C. L. Bottasso. «Wind tunnel testing of a closed-loop wake deflection controller for wind farm power maximization». In: *Journal of Physics: Conference Series* 753.3 (2016) (cit. on pp. 39–42).

[44] C. L. Bottasso and F. Campagnolo. *Wind Tunnel Testing of Wind Turbines and Farms*. Springer International Publishing, 2022 (cit. on pp. 39, 41).

[45] A.C. Bertolino, A. De Martin, A. Nesci, and M. Sorli. *Meccatronica - Analisi, progettazione e modellazione di servosistemi*. Torino, ITA: CLUT Editrice, 2021 (cit. on pp. 43, 61, 66, 69, 70).

[46] Mühle and Laureys. «Calibration of the G1 wind turbine». In: (2021) (cit. on pp. 44, 47, 48, 50).

[47] H. Kozmar. «Influence of spacing between buildings on wind characteristics above rural and suburban areas». In: *Wind and Structures* 11 (2008) (cit. on p. 53).

[48] H. Sarlak, T. Nishino, L. Martínez-Tossas, C. Meneveau, and J. Sørensen. «Assessment of blockage effects on the wake characteristics and power of wind turbines». In: *Renewable Energy* 93 (2016) (cit. on p. 54).

[49] F. Campagnolo, F. Castellani, F. Natili, D. Astolfi, and F. Mühle. «Wind tunnel testing of yaw by individual pitch control applied to wake steering». In: *Frontiers in Energy Research* 10 (2022) (cit. on p. 54).

[50] C. Wang, F. Campagnolo, H. Canet, D. J. Barreiro, and C. L. Bottasso. «How realistic are the wakes of scaled wind turbine models?» In: *Wind Energ. Sci.* 6 (2021) (cit. on p. 60).

[51] Thrust Flight. *https://www.thrustflight.com/pitot-tube-static-air-system/* (cit. on p. 62).